Characterizing Thermohaline Intrusions in the North Pacific Subtropical Frontal Zone

ANDREY Y. SHCHERBINA, MICHAEL C. GREGG, MATTHEW H. ALFORD, AND
RAMSEY R. HARCOURT

Applied Physics Laboratory, University of Washington, Seattle, Washington

ABSTRACT

A monthlong field survey in July 2007, focused on the North Pacific subtropical frontal zone (STFZ) near 30°N, 158°W, combined towed depth-cycling conductivity–temperature–depth (CTD) profiling with shipboard current observations. Measurements were used to investigate the distribution and structure of thermohaline intrusions. The study revealed that local extrema of vertical salinity profiles, often used as intrusion indicators, were only a subset of a wider class of distortions in thermohaline fields due to interleaving processes. A new method to investigate interleaving based on diapycnal spiciness curvature was used to describe an expanded class of laterally coherent intrusions. STFZ intrusions were characterized by their overall statistics and by a number of case studies. Thermohaline interleaving was particularly intense within 5 km of two partially compensated fronts, where intrusions with both positive and negative salinity anomalies were widespread. The vertical and cross-frontal scales of the intrusions were on the order of 10 m and 5 km, respectively. Though highly variable, the slopes of these features were typically intermediate between those of isopycnals and isohalines. Although the influence of double-diffusive processes sometime during the evolution of intrusions could not be excluded, the broad spectrum of the observed features suggests that any role of double diffusion was secondary.

1. Introduction

Definitions of thermohaline intrusions vary among researchers and are often related to temperature or salinity inversions (e.g., Ruddick et al. 1999; Ruddick and Kerr 2003). The variety of definitions arises from the need to accommodate two loosely related properties of these features:

1) They are formed by local lateral intrusion of one water mass into another at a particular depth.
2) They tend to produce inversions—that is, changes of sign of vertical temperature or salinity gradients.

Some researchers avoid the term ''intrusion'' and restrict discussion to ''inversions'' or ''interleaving'' (May and Kelley 1997, hereafter MK97). Others use the terms ''intrusion'' and ''interleaving'' interchangeably (Mueller et al. 2007). However, interleaving motion does not necessarily produce inversions, nor do inversions automatically imply lateral interleaving. Studies of interleaving driven by double diffusion (DD) may have contributed to the confusion since inversions are necessary for formation of that particular class of intrusions. Equating intrusions with inversions also implies that subsurface extrema in conductivity–temperature–depth profiles mark the cores of intrusions (Toole 1981). Here we show that this assumption is not generally valid.

To move beyond semantics, one might ask a broader question: Why are we interested in these features? Thermohaline intrusions are of interest because they may indicate lateral exchange between water masses (Stommel and Fedorov 1967; Joyce 1977), which supports defining intrusions as vertical variations in stratification arising from the layered interleaving of hydrographically disparate water masses. With this approach, inversion of temperature or salinity trends is not a crucial feature of an intrusion, although it is understood that such an inversion can alter the dynamics of interleaving through double-diffusive effects. It is then necessary to develop an objective method to detect intrusions as vertical water mass transitions. Here, we use diapycnal spiciness curvature as a generalized intrusion detector (section 4).

Corresponding author address: Andrey Shcherbina, APL, University of Washington, 1013 NE 40th St., Seattle, WA 98105.
E-mail: ashcherbina@apl.washington.edu

The North Pacific subtropical frontal zone (STFZ), centered around 30°N, is known as a site of a wide variety of thermohaline interleaving features (Roden 1981; Yuan and Talley 1992). In summer 2007 an extensive field program was undertaken to characterize the three-dimensional structure of thermohaline intrusions, establish their relationship with the thermohaline fronts and other mesoscale features, and gain insight into their evolution and dynamics (section 2). Rigorous methods to detect and describe the intrusions in a single hydrographic profile, a section, or a quasi-3D survey were developed. Section 3 provides a brief review of traditional analysis methods; a new and improved method, developed for the present study, is described in section 4. A detailed description of the thermohaline intrusion field and the structure of individual features observed in July 2007 is given in sections 5–8. Possible formation mechanisms and implications for lateral water mass exchange are discussed in section 9.

2. Observations

a. Data collection

A field study of the interleaving features in the STFZ near 31°N, 158°W was conducted 5–29 July 2007 onboard the R/V *Wecoma*. The STF07 experiment encompassed hydrographic surveying, microstructure profiling, shipboard velocity observations, and Lagrangian float releases. The present study focuses on hydrographic and shipboard observations exclusively.

The hydographic survey was conducted with the Shallow Water Integrated Mapping System (SWIMS), a depth-cycling towed instrument platform. SWIMS instrumentation consisted of two Sea-Bird conductivity–temperature–depth (CTD) units with additional dissolved oxygen and chlorophyll fluorescence sensors, and a pair of 300-kHz acoustic Doppler current profilers (ADCPs). SWIMS was towed, typically at 6 kt, undulating between two predetermined depths within the upper 200 m. Depending on the profiling depth range and ship speed, horizontal separation between parallel tracks of the sawtooth pattern was 0.4–2 km. The main source of errors in the hydrographic observations was the uncertainty of the salinity measurements due to temporal mismatch in response of temperature and conductivity probes (salinity spiking and thermal mass effect). These effects can be reduced substantially using appropriate filters for temperature and conductivity signals (Morison et al. 1994; Ferrari and Rudnick 2000). The remaining rms salinity error was estimated to be of order 5×10^{-4}.

The SWIMS tow patterns included long straight sections, "radiator," and star-shaped patterns (Fig. 1). A total
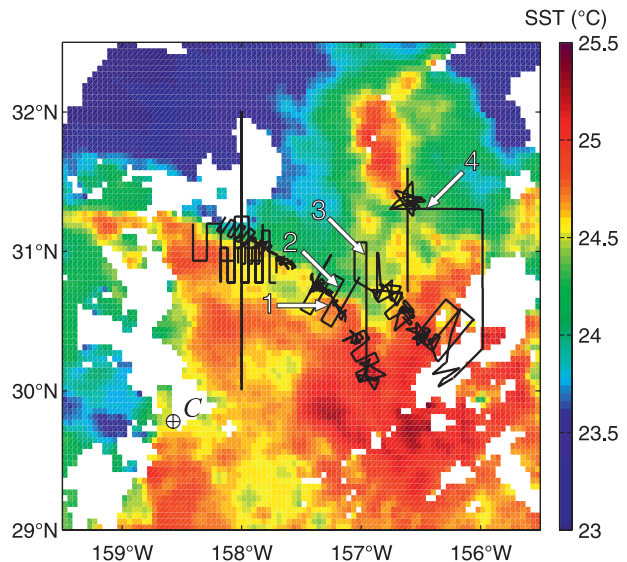

FIG. 1. SWIMS survey lines from 5 to 29 Jul 2007. Background shows sea surface temperature on 7 Jul 2007, based on Moderate Resolution Imaging Spectroradiometer (MODIS) *Aqua* imagery [courtesy of NASA Jet Propulsion Laboratory (JPL) Physical Oceanography Distributed Active Archive Centre (PO.DAAC)]. Numbered arrows indicate features detailed in Figs. 10, 11.

of 32 patterns or "groups" were executed, with more than 11 000 profiles spanning a cumulative survey length of 4500 km. The location, shape, and size of the tow patterns were adapted during the cruise, allowing focused sampling of observed features. Most of the patterns were intentionally distorted to account for the projected water mass advection over the duration of the tow. This approach allowed greater control over the resulting survey track in the advected frame of reference.

The overall survey was guided by near-real-time sea surface temperature (SST) imagery, whenever available (Fig. 1). Even though the thermocline stratification was heavily capped by seasonal warming, there was sufficient correspondence of the surface temperature features with the structure of the thermocline fronts to make SST imagery useful in focusing the observations.

R/V *Wecoma* was equipped with 150- and 75-kHz ADCPs, providing underway velocity observations. The present study uses data from the short-range 150-kHz system, covering the upper 150 m of the water column with 4-m vertical resolution and 2-min ensembles. Underway ADCP data were collected and processed by the University of Hawaii data acquisition system (UHDAS).

b. STFZ oceanography

The North Pacific STFZ is a wide (28°–35°N) transition that separates North Pacific Central Water to the south from cooler and fresher waters of subpolar origin

to the north (Roden 1980). Both temperature and salinity in the upper 500 m of the STFZ increase toward the surface and toward the south (Figs. 2a,b). As a result the layer is potentially susceptible to salt-fingering instability (Schmitt 2003), though no direct evidence of double diffusion, such as staircase structuring, was observed in this area.

Within the STFZ, several sharp, partially compensated thermohaline fronts are typically observed in the upper 200 m. Horizontal thermohaline gradients are thought to be created by spatially varying heat and freshwater fluxes in the North Pacific, while wind-driven differential advection serves as a mechanism of frontogenesis (Roden 1980; Takeuchi 1984). Roden specifically mentions that "agreement exists between the location of the thermohaline fronts and regions of large vertical velocity gradients produced by the geographical variations of the curl of the wind stress."

During the STF07 experiment, at least two distinct fronts (F1 and F2) were traversed (Fig. 2). At the time of the transect, the fronts were most evident in salinity between 40- and 100-m depth: one at about 31°N (F1) and another at about 31°20′N (F2). The southern front, F1, was nearly vertical, while the horizontal position of the northern one, F2, changed by 12 km over the vertical extent of 50 m, a slope of roughly 4×10^{-3}. Thermohaline fields in the study area were distorted by a mesoscale meander, partially visible in the SST imagery (Fig. 1). According to shipboard observations and a concurrent Lagrangian float drift, the flow generally followed a broad circular arc about a center located to the southeast at 29°45′N, 158°32′W. The two fronts, F1 and F2, were located approximately 160 and 200 km from the center of the arc, respectively. Tangential advection along this arc was on the order of 0.3 m s^{-1} near the surface, decreasing to 0.1 m s^{-1} below 250 m. Radial advection was between −0.1 and +0.1 m s^{-1}. Consistent with the thermal wind balance, isopycnals were shoaling toward the outside of the meander (Fig. 2c), producing a maximum isopycnal slope of 2×10^{-3} below 100 m in the vicinity of F1 and F2, between 30°50′ and 31°30′N. A strong alongfront jet with the subsurface velocity maximum of 0.4 m s^{-1} was also observed in this region (Fig. 2f).

Dissolved oxygen concentration (Fig. 2d) was higher in the seasonal thermocline (40−120 m) than in the mixed layer and the permanent thermocline below 140 m. It also increased toward the outside (cold) side of the meander, with abrupt steps across the F1 and F2 fronts. Distribution of oxygen content was distinctively patchy, with alternating vertical tongues of high and low oxygen content throughout the frontal zone. Similar patchiness was observed in Chl-*a* fluorescence (Fig. 2e).

These features suggest strong variability of vertical advection in the STFZ.

3. Traditional intrusion detection methods

The simplest method of detecting intrusions—dating back to Roden (1964), Fedorov (1978), Gregg (1975)—consists of identifying isolated reversals of large-scale vertical trends in salinity (or temperature). Each inversion would be bounded by two local extrema—a minimum and a maximum. One of them is taken to represent the intrusion's core, the other its lower or upper boundary. This designation is generally ambiguous, although ambiguity can sometimes be avoided in certain well-defined situations, such as thin and isolated intrusions disturbing a known background profile. This method aims to reproduce visual identification of intrusions, seen clearly as local extrema in profiles of some property (e.g., salinity) versus some vertical coordinate (depth or density). Though easily visualized, the method is difficult to formalize as it is prone to false-negative results owing to noise or small-scale intrusions (see also section 3c).

a. Anomaly method

McDougall and Giles (1987), henceforth McDG87, show that extrema of temperature or salinity are not reliable proxies for the intrusion location. McDG87 emphasize that the location (and even the presence) of extrema in temperature or salinity profiles depends on the shape of unperturbed profiles and also show that both the lateral and vertical mixing may result in an apparent vertical shift of the extrema. As an alternative, McDG87 suggest an isopycnal salinity (or spiciness) anomaly as an indicator of the intrusion strength, where the anomaly is computed relative to some "mean background state" of the ocean.

There are several possible choices for defining this background state: low-pass filtering, temporal averaging, or using the observational data that are deemed intrusion free. However, the choice of a particular background definition to some extent determines which features will be classified as intrusions: for example, the base of the mixed layer, an internal wave, or a sloping front may or may not result in an anomaly relative to different background definitions.

b. Scale sensitivity

Owing to inherent noisiness of hydrographic data, any algorithm of intrusion detection based on finding local extrema of temperature, salinity, spiciness, or other variables requires prefiltering of raw profiles to mitigate false peak detection. One of the undesirable effects of profile smoothing is the shifting of peak locations and
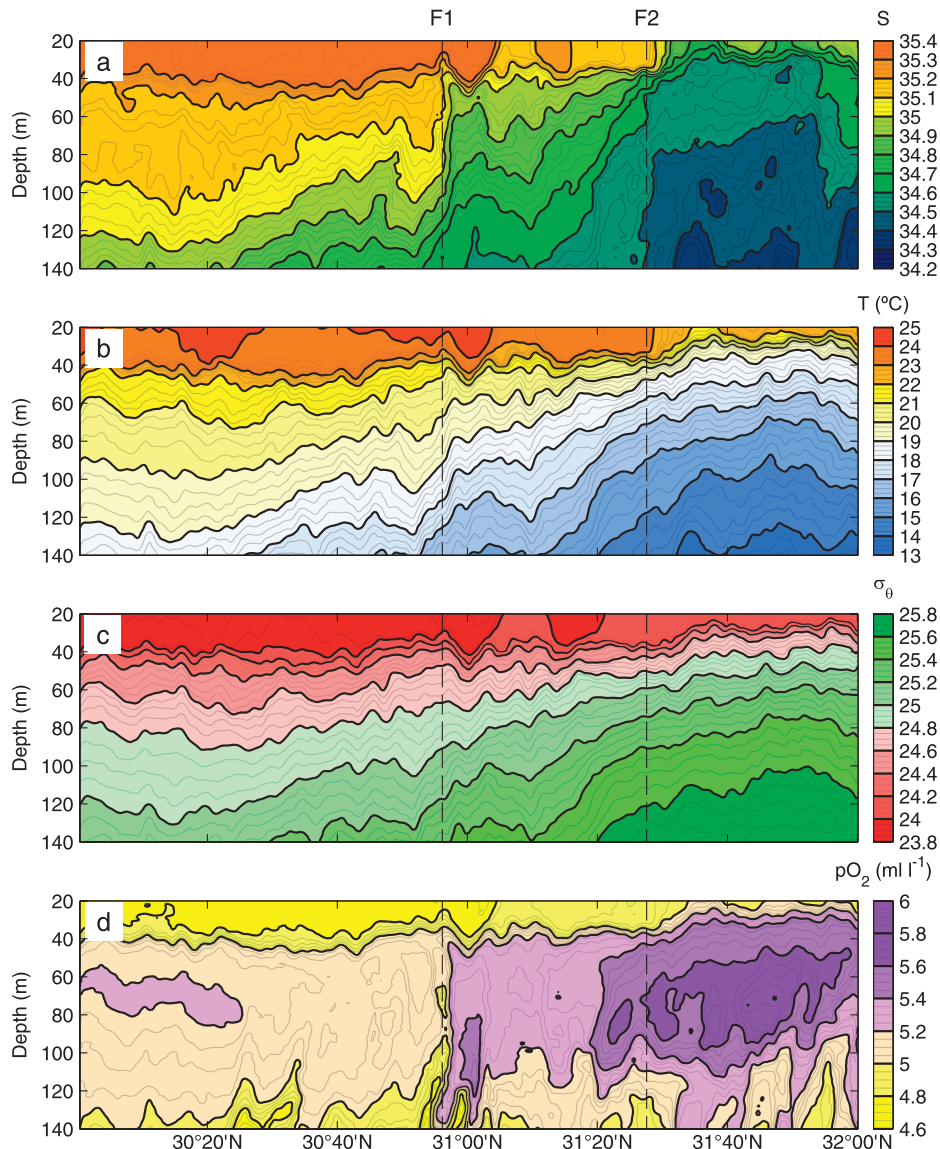
FIG. 2. Distribution of (a) salinity, (b) temperature, (c) density, and (d) dissolved oxygen concentration along 158°W based on SWIMS survey 6 Jul 2007. Vertical dashed lines mark the approximate location of the two thermohaline fronts F1 and F2.

amplitudes with respect to their unsmoothed realizations. This effect can be eliminated by using multiscale peak analysis, which derives the peak parameters from the raw profile, but uses its smoothed version to filter out the spurious extrema (see appendix A).

A more fundamental problem that appears unavoidable is that whether peaks are considered "real" depends critically on the parameters of profile smoothing that can rarely be chosen objectively. Such a dependence of the population of the detected peaks on the scale of prefiltering is illustrated in Fig. 3 using a typical salinity section obtained during STF07 as an example.

Shifting of the peaks arising from prefiltering is avoided using the multiscale peak analysis algorithm (appendix A), allowing direct comparison of detection of individual peaks at various scales of filtering, L.

The relative density of the peaks in various parts of the section appears to be largely independent on the scale L of the analysis. On the other hand, because the distribution of salinity variance in the regions of interleaving tends to be dominated by a large number of small features, the number of detected intrusions falls rapidly with increasing L. It should be emphasized that owing to the multiscale analysis algorithm used here, the locations of
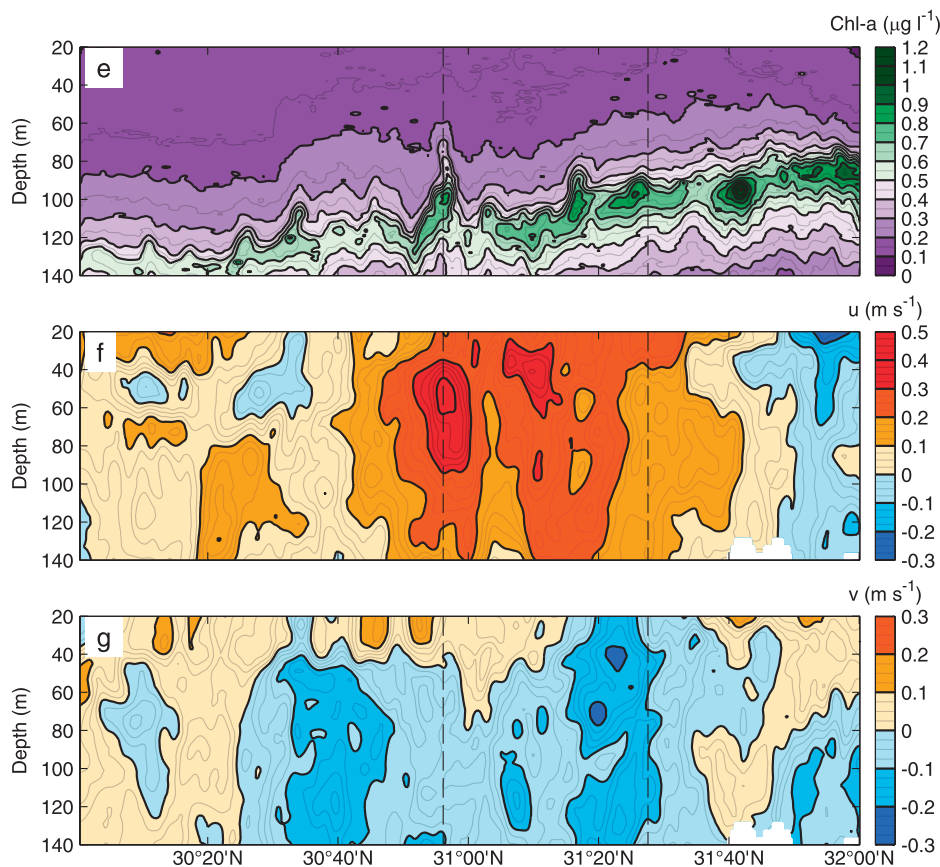
FIG. 2. (*Continued*) Distribution of (e) Chl-a fluorescence, (f) zonal velocity (positive east), and (g) meridional velocity (positive north) along 158°W based on SWIMS and shipboard ADCP survey 6 Jul 2007. Vertical dashed lines mark the approximate location of two thermohaline fronts (F1 and F2).

the peaks do not change with increasing L, as they are determined from the unsmoothed profiles. Instead, the peak rejection criteria become stricter as L increases.

Because the thickness and the amplitude of each peak are defined relative to the adjacent extrema, these values may change depending on which particular extrema are retained by the algorithm. In a particular population of extrema, shown in Fig. 3, 62% of the prominent ($L = 20$ m) peaks appear thicker than the corresponding peaks analyzed with $L = 3$ m. At the same time, 32% of the peaks have the same properties regardless of the scale of the analysis ($L = 3$–20 m). The remaining 6% of the peaks appear thinner according to a larger-scale ($L = 20$ m) analysis. The latter finding is somewhat counterintuitive and arises only in a small number of asymmetric peaks with a particular shape.

The pronounced shift in the distribution of peak thicknesses due to variations in L is illustrated in Fig. 4a. Even though the peaks are not explicitly filtered based on their size, most of the retained peaks have a thickness comparable to L (Figs. 4a,b). Mean amplitude of the

detected peaks also scales well with L (Fig. 4b). The latter result is expected, as peak thickness and amplitude tend to be well correlated (with a nearly 100% significant correlation coefficient of 0.25–0.65, depending on L).

The implication of this result is that magnitudes and sizes of intrusions characterized by any of the peak-analysis methods are, to a large extent, a reflection of subjective choices in analysis procedures rather than an objective characterization of the actual interleaving field. In absence of a clear separation of scales, the peak analysis procedure must be tuned arbitrarily to focus on a particular range of features. Consequently, a comprehensive investigation of the field of features is necessary as a preliminary step. A dynamically justified method of characterization of the interleaving field as a whole is suggested in the next section.

4. Diapycnal spiciness curvature: A new intrusion indicator

To avoid the pitfalls of ad hoc background selection and improve the dynamical rationale of intrusion
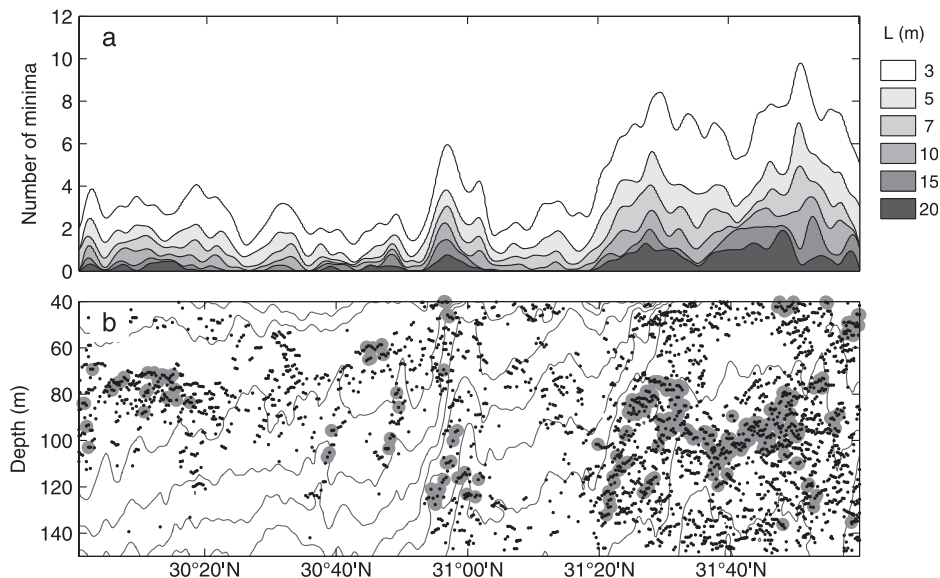
FIG. 3. Sensitivity of the peak detection algorithm to the scale of the analysis, L. (a) Dependence of the average per-profile number of detected salinity minima on the scale of the analysis. (b) Salinity section along 158°W with the locations of the minima detected with the small ($L = 3$ m, dots) and large ($L = 20$ m, gray circles) scale of the analysis.

localization, we suggest diapycnal spiciness curvature (defined below) as a parameter characterizing the local strength of interleaving. Justification for this approach lies in the observation that the intrusions are associated with the points of increased curvature (''kinks'') of a θ–S diagram (Fig. 5a).

For the purpose of this study, spiciness τ is defined through its differential

$$d\tau = \rho(\alpha\,d\theta + \beta\,dS), \qquad (1)$$

where ρ is the density, and $\alpha = -\rho^{-1}(\partial\rho/\partial\theta)$ and $\beta = \rho^{-1}(\partial\rho/\partial S)$ are the coefficients of thermal expansion and saline contraction, respectively. Construction of a particular globally consistent solution of (1) is not essential here, although the formulation of Flament (2002) can be used for practical purposes.
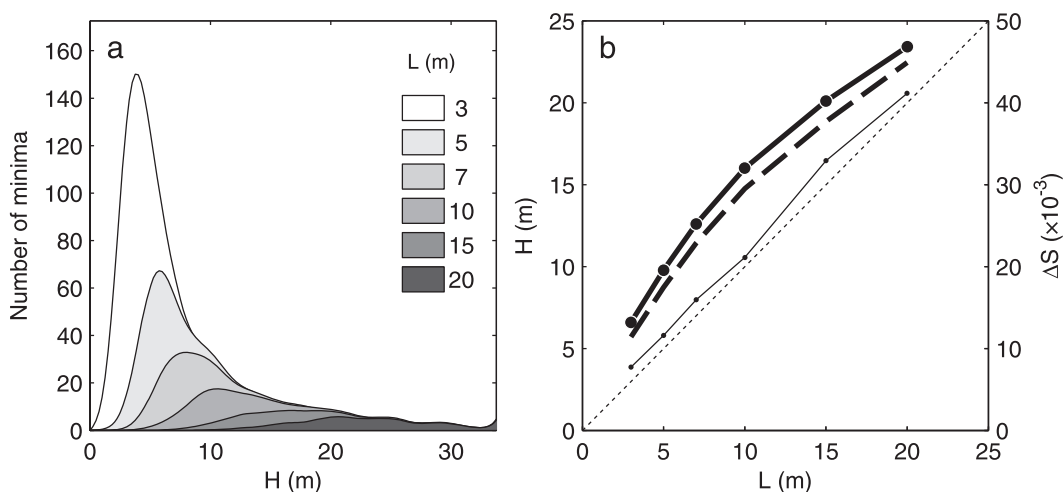

FIG. 4. (a) Distribution of peak thickness H (vertical extent) for different scales L of the analysis. (b) Dependence of the mean (thick line) and most probable (thin line) values of peak thickness, as well as the mean peak amplitude ΔS (heavy dashed line) on the scale of analysis. Multiscale analysis of salinity minima peaks was applied to the salinity section along 158°W, also shown in Fig. 3b.
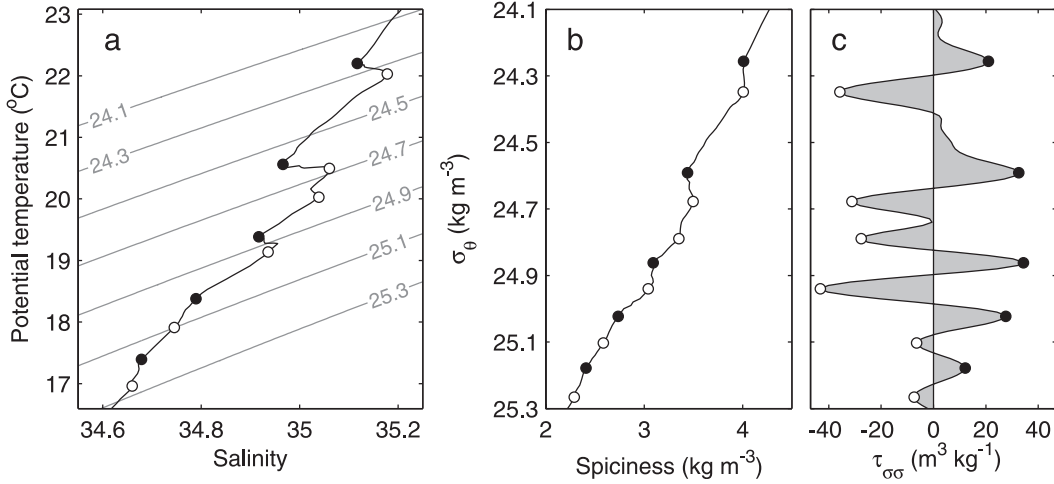
FIG. 5. An example of interleaving effects on (a) θ–S diagram as well as the vertical profiles of (b) spiciness τ and (c) diapycnal spiciness curvature (low passed with Blackman filter with half width of 0.1 σ_θ). Most prominent curvature minima and maxima are marked with open and solid circles, respectively. Profiles were obtained during SWIMS survey on 17 Jul 2007 at 30°30.34′N, 157°20.02′W, at a point corresponding to $x = 11$ km in Fig. 11. Absolute spiciness was calculated following the Flament (2002) method.

Dynamical significance of the second derivative of spiciness with respect to potential density along a vertical cast can be clarified by considering the "water mass transformation" equations, which describe the evolution of salinity and potential temperature in isopycnal coordinates (McDougall 1984; Zika and McDougall 2008):

$$S_t + \mathbf{V}\nabla S = D\rho\alpha\sigma_z^{-1}(S_z\theta_{zz} - \theta_z S_{zz}) + (\text{IM}S), \quad (2)$$

$$\theta_t + \mathbf{V}\nabla\theta = D\rho\beta\sigma_z^{-1}(S_z\theta_{zz} - \theta_z S_{zz}) + (\text{IM}\theta), \quad (3)$$

where subscripts indicate differentiation, $\mathbf{V}$ is the isopycnal advection velocity, D is a diapycnal eddy diffusivity, and z is the diapycnal coordinate; (IMS) and (IMθ) abbreviate the isopycnal mixing terms. A linear combination of (2) and (3) produces a similar equation for spiciness:

$$\tau_t + \mathbf{V}\nabla\tau = 2D\rho^2\alpha\beta\sigma_z^{-1}(S_z\theta_{zz} - \theta_z S_{zz}) + (\text{IM}\tau). \quad (4)$$

The first term on the right side of (4) describes diapycnal processes. This term is equivalent to $D\sigma_z^2\tau_{\sigma\sigma}$, where $\tau_{\sigma\sigma} \equiv (d^2\tau/d\sigma^2)_{\text{prof}}$ is the second derivative of spiciness with respect to potential density along a profile (diapycnal spiciness curvature),

$$\left(\frac{d^2\tau}{d\sigma^2}\right)_{\text{prof}} = \sigma_z^{-1}\frac{d}{dz}\left(\frac{\alpha\theta_z + \beta S_z}{-\alpha\theta_z + \beta S_z}\right)$$
$$= 2\rho^2\alpha\beta\frac{S_z\theta_{zz} - \theta_z S_{zz}}{\sigma_z^3}. \quad (5)$$

Notice that, in the derivation of (5), vertical variation of α and β does not have to be neglected.

Incidentally, $\tau_{\sigma\sigma}$ varies similarly to the curvature of a profile on an $\alpha\theta$–βS diagram, given by

$$\kappa = \alpha\beta\frac{\theta_z S_{zz} - \theta_{zz} S_z}{(\alpha^2\theta_z^2 + \beta^2 S_z^2)^{3/2}}, \quad (6)$$

which aids its intuitive interpretation. Also, it should be noted that

$$\tau_\sigma \equiv \frac{1 + R_\rho}{1 - R_\rho} \equiv -\tan\text{Tu}, \quad (7)$$

where $R_\rho \equiv (\alpha\theta_z)/(\beta S_z)$ is the vertical density ratio and Tu $= \tan^{-1}[(\alpha\theta_z + \beta S_z)/(\alpha\theta_z - \beta S_z)]$ is the Turner angle (Ruddick 1983), and thus $\tau_{\sigma\sigma} = d(\tan\text{Tu})/d\sigma$. Lastly, it can be shown that if $\alpha_z\theta_z \ll \alpha\theta_{zz}$ and $\beta_z S_z \ll \beta S_{zz}$ (both conditions are typically satisfied in the ocean), the following approximate relationships hold:

$$\tau_{\sigma\sigma} \approx 2\beta\rho S_{\sigma\sigma} \approx 2\alpha\rho\theta_{\sigma\sigma}. \quad (8)$$

Diapycnal curvature $\tau_{\sigma\sigma}$ is a good indicator of water mass interleaving. In absence of lateral advection, diapycnal mixing eventually destroys the curvature of the vertical profiles, leading to $\tau_{\sigma\sigma} = 0$. As a result, the vertical density ratio $R_\rho = (\tau_\sigma - 1)/(\tau_\sigma + 1)$ of an established water mass tends to be constant (Schmitt 1981). Conversely, high absolute curvature $|\tau_{\sigma\sigma}|$ indicates a sharp diapycnal interface between dissimilar water masses, often occurring as a result of ongoing or recent differential lateral advection, that is, water mass intrusion.

The shape of the spiciness profiles affected by interleaving motions depends on many factors, including

variations in diapycnal diffusivity D, diapycnal and isopycnal gradients, and the advection history. As a result, the number and sequence of extrema associated with a particular intrusion may also vary (Fig. 6). A typical low-salinity intrusion (Fig. 6a) exhibits a strong positive peak of $\tau_{\sigma\sigma}$, surrounded by two weaker negative peaks. The "core" of the intrusion (i.e., the layer of strongest advection) can be expected to lie close to the level of maximum curvature $|\tau_{\sigma\sigma}|$, but exact correspondence should not be implied. If the vertical extent and lateral displacement of an intrusion are sufficiently large, a special case of a "thick" intrusion can be realized (Fig. 6b). In this case, the intrusion core is marked by two curvature extrema of the same sign. As shown by a synthetic example (appendix B), an intrusion can morph from thick to thin configurations and back as it is followed laterally; splitting of the central curvature maximum may then be observed (see Fig. B1b). In the case of a series of counterflowing intrusions (Fig. 6c), curvature extrema of opposite signs mark the core of each of the layers.

Using the curvature parameter $\tau_{\sigma\sigma}$ to characterize water mass interleaving offers several advantages:

1) Unlike salinity or temperature extrema, $\tau_{\sigma\sigma}$ is directly relevant to the dynamics of water mass evolution (4).
2) $\tau_{\sigma\sigma}$ is not affected by the background stratification of water masses.
3) $\tau_{\sigma\sigma}$ is not affected by the strain or vertical displacement caused by internal waves, but retains intrusions produced by internal wave shear.
4) Unlike the anomaly method, no subjective definition of the background profile is required.

The related $\alpha\theta$–βS diagram curvature parameter κ shares many of the same advantages, but it is somewhat more difficult to estimate robustly from the observations, especially if both temperature and salinity have occasional inversions.

Side-by-side comparison of inversion- and curvature-based intrusion detection methods in a synthetic example (appendix B) showed that the latter method is substantially more sensitive, especially where the intrusion structure is complicated by strong vertical gradients. The intrusion core was also located more accurately. Local curvature extrema in a σ–τ (or $\alpha\theta$–βS) profile approximate the locations of strongest instantaneous isopycnal advection of properties. Consequently, intrusion detection methods based on curvature are inherently different from the anomaly tracking methods, as the latter focus on the bulk effect of property advection within individual intrusions. Combined analysis of the curvature and the anomaly fields gives a more comprehensive description of interleaving features: the former clearly
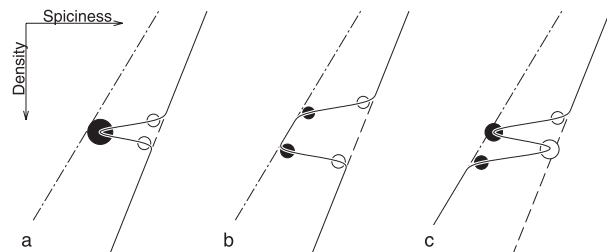

FIG. 6. Schematic salinity profiles (thin solid lines) representing various forms of interleaving between two water masses shown as dashed and dashed–dotted lines. Cases are (a) thin, (b) thick, and (c) alternating intrusions. Open (solid) circles mark the negative (positive) extrema of spiciness curvature $\tau_{\sigma\sigma}$; size of the circles is proportional to the maximum values of $|\tau_{\sigma\sigma}|$.

shows small disturbances of the water mass structure, whereas the latter highlights the disturbances that result from sustained, coherent growth.

It should be noted that vertical disparity of water mass stratification can also result from diapycnal processes rather than lateral interleaving activity. This would likely occur in areas of active water mass formation by surface heat or salt fluxes. Initially sharp diapycnal interfaces at the lower extent of a newly formed water mass can be expected to weaken with time elapsed after the most recent ventilation due to mixing. A weak curvature signature marking the extent of deep winter ventilation was observed during the present study alongside the intrusive features (see section 5a).

Containing a second derivative, diapycnal spiciness curvature is inherently sensitive to high-frequency noise in the measured fields. Standard error of spiciness, $SE(\tau)$, gridded in $\Delta\sigma = 0.01$ kg m^{-3} potential density bins was on the order of 4×10^{-3} kg m^{-3}. Assuming a normal distribution of errors and their lack of bin-to-bin correlation, the standard error of the finite-difference estimate of spiciness curvature is $SE(\tau_{\sigma\sigma}) = 6^{1/2} SE(\tau)/\Delta\sigma^2 \approx 90$ m^3 kg^{-1}. This presents a problem because the typical rms $\tau_{\sigma\sigma}$ is of the same order of magnitude and thus the signal-to-noise ratio is very low. Smoothing of the raw gridded spiciness profiles using a Blackman low-pass filter with half width of 0.08 kg m^{-3} (8 grid points) improves the signal-to-noise ratio to $O(10)$, which is sufficient for clear identification of the curvature features. At this level of smoothing, the estimated rms error of spiciness curvature is $O(1$ m^3 kg$^{-1})$.

5. Diapycnal spiciness curvature distribution in the STFZ

a. Section view

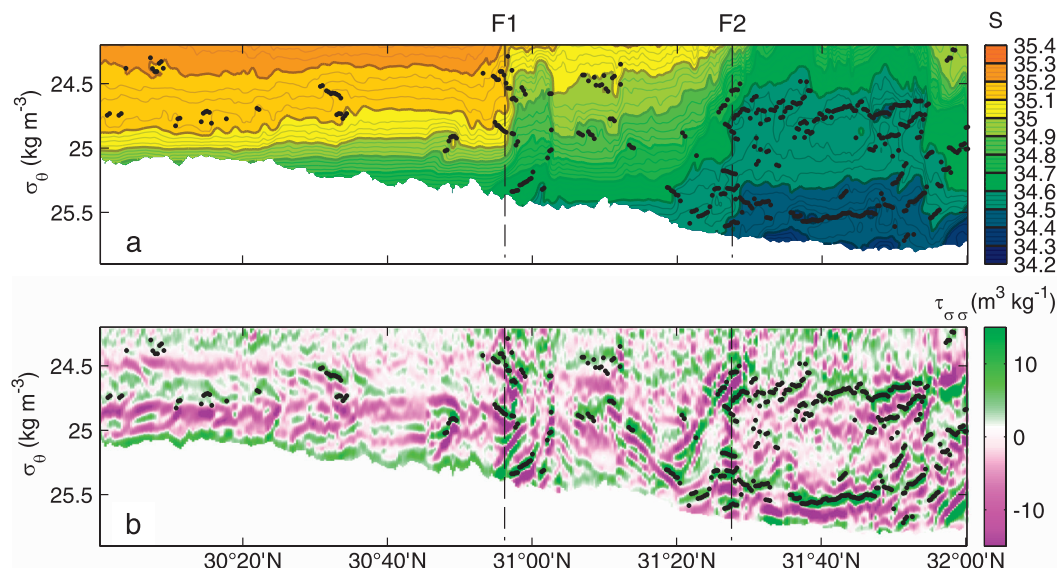The STFZ survey in July 2007 included several long (>200 km) meridional SWIMS sections, particularly

FIG. 7. Distribution of (a) salinity and (b) diapycnal spiciness curvature, $\tau_{\sigma\sigma}$, on a north–south section along 158°W (Fig. 2). Vertical dashed lines mark the approximate location of fronts F1 and F2; black dots mark salinity minima.

suitable for investigating the variability of intrusions across the frontal zone. One of these sections occupied on 6 July 2007 along 158°W crossed both thermohaline fronts in the region and sampled water masses that typified the STFZ during the experiment (see section 2b, Fig. 2). This transect contained numerous salinity inversions, suggestive of thermohaline intrusions. For analysis, the section is presented in an isopycnal coordinate system (Fig. 7), which reduces the distortion of interleaving features by internal waves.

The North Pacific Central Water mass in the southern part of the section is largely homogeneous laterally. The vertical density ratio in that region varies smoothly between 5 and 10, and $\tau_{\sigma\sigma}$ is small (Fig. 7b), as expected for a stable water mass. Variations of curvature observed there are nonetheless significant compared to the expected rms error of 1 m³ kg⁻¹ (Fig. 8a). For example, a weak negative curvature extremum at $\sigma_\theta = 24.85$ kg m⁻³ (which corresponds to a depth of about 85 m) marks the lower boundary of a restratified winter mixed layer and its transition into the main thermocline where the vertical density ratio becomes nearly constant ($R_\rho = 2.75$, $\tau_{\sigma\sigma} = 0$).

North of about 30°55′N, the section crosses a succession of thermohaline fronts (F1 and F2 in Fig. 7), as well as several smaller features with lateral gradient reversals (at 31°03′ and 31°55′N). The section shown did not extend north of the STFZ, so no evidence of a laterally coherent water mass was found in this part of the section.

Strong interleaving, characterized by alternating patches of high and low curvature, $\tau_{\sigma\sigma}$, is evident in the

vicinity of the fronts and, to a lesser degree, north of them (Figs. 7c, 8a). In this section rms diapycnal spiciness curvature is elevated about threefold within 1–2 km of the two fronts. The observed cross-front variations are statistically significant, given the expected rms curvature error $O(1$ m³ kg⁻¹).

Interleaving patches are organized in bands that are laterally coherent for at least 10–20 km. These coherent bands cross isopycnals, isobars, isohalines, and each other. Their cross-isopycnal slope varies from -6×10^{-5} to $+4 \times 10^{-5}$ kg m⁻⁴ between different features. These slopes appear to vary more between the patches than within each individual feature. Cross-isobar slopes were more uneven due to isopycnal heaving, typically varying between $\pm 8 \times 10^{-3}$, which correspond to the phase angles of internal waves with frequencies less than $2f$. This estimate is given only for reference; we do not posit any relationship between the observed features and internal waves.

Several clusters of nearly isopycnal intrusions were located next to the fronts (30°57′N, F1; 31°03′, 31°27′N, F2). Notice that these features are more limited laterally (<5 km) than the sloping features mentioned previously. At the same time, they exhibit higher curvatures and show stronger vertical coherence (up to five full oscillations from minimum negative to maximum positive curvature). Intensified variance of curvature $\tau_{\sigma\sigma}$ in the front can be explained by the increase in isopycnal salinity gradients (Fig. 8c). No corresponding increase in rms vertical shear V_z^{rms} was measurable in the upper 150 m in this area (Fig. 8b), although a marked increase
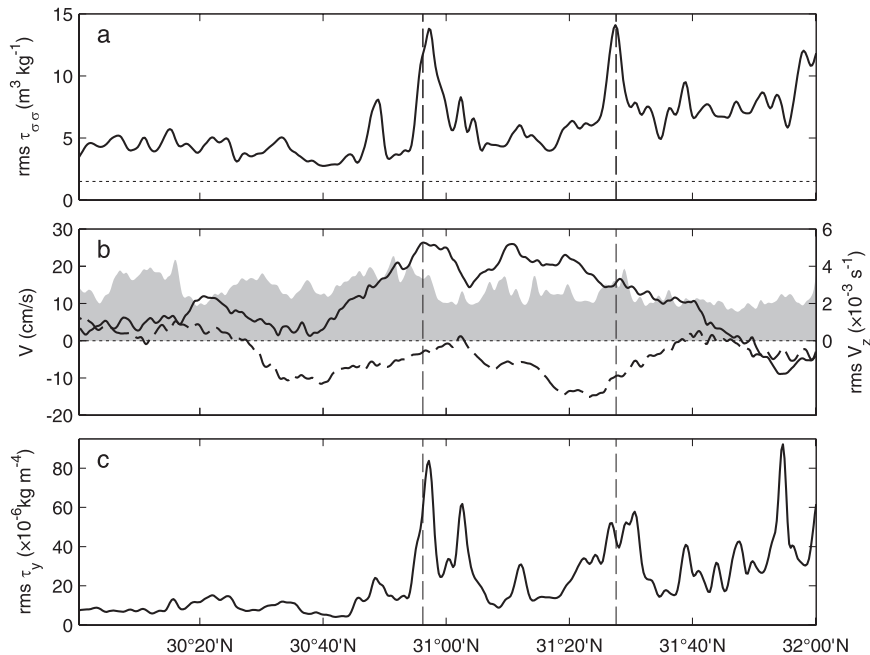
FIG. 8. Distribution of (a) rms diapycnal spiciness curvature, (b) vertically averaged eastward and northward velocities (solid and dashed black lines, respectively) and rms 4-m shear (gray shading), and (c) rms isopycnal along-section spiciness gradient on a section along 158°W (Fig. 7). Vertical dashed lines mark the approximate location of fronts F1 and F2. Vertical averages and rms values were computed over the potential density range 23.8–25.8 kg m^{-3}. The horizontal dotted line in (a) marks the uncertainty estimate for $\tau_{\sigma\sigma}$.

in shear variance was noted below 200 m in the STFZ (not shown). Barotropic and low-vertical-mode flow is strongest in the vicinity of the two baroclinic fronts.

b. Mesoscale view

The analysis of cross-section variability of the diapycnal curvature field (Fig. 7c and Fig. 8a) can be extended using the entire set of SWIMS data. A total of 32 individual SWIMS surveys with various tow lengths and survey patterns during 5–29 July were synthesized by averaging the observations in 5 km × 5 km spatial bins (Fig. 9). A 45° arc of a mesoscale meander was covered during this 25-day period. Along the curve of this meander, two thermohaline fronts, evident as sharp discontinuities in isopycnal salinity (Fig. 9a), correspond to F1 and F2 (Fig. 7 and Fig. 8). Enhanced interleaving was found in a pair of 10-km-wide bands aligned with these two fronts, where the rms diapycnal curvature was elevated by a factor of 2–3 over the levels outside the frontal zone. The area between the fronts was characterized by intermediate curvature variance.

6. Examples of observed intrusions

During the survey, a wide variety of interleaving features was observed, of which a few examples are shown

in Figs. 10 and 11. The range of feature characteristics is broad, and very few universal traits can be identified. Most were found within the seasonal thermocline at depths between 50 and 120 m and were laterally coherent for up to 10–20 km. They extended vertically over $\sim 0.3\sigma_\theta$ or ~ 5 m between the $\tau_{\sigma\sigma}$ extrema; thicker features (>20 m) showed secondary internal folding (Fig. 11a). Intersections and branching of features with different slopes were occasionally observed (Figs. 10a,b). Both attached (Fig. 10a) and isolated features (Fig. 11a) were found, but the latter may represent a slice perpendicular to the interleaving axis. The presence of both types of features (Fig. 11a) suggests variations in the orientation of interleaving axes.

Typical vertical profiles through the intrusions (Fig. 12) show a weak temperature signal but substantial salinity variability. Extrema in both salinity and $\tau_{\sigma\sigma}$ mark most of the features, but the $\tau_{\sigma\sigma}$ signature of the interleaving features typically extends beyond the salinity inversion patches (Fig. 10d). Consequently, observed inversions are a particular case of θ–S field distortion that exceed background salinity stratification. See appendix C for the discussion on when an intrusion becomes an inversion.

Velocity variations at vertical scales similar to those of the intrusions were common in the STFZ (Fig. 10 and Figs. 11c,d,g,h). Occasionally, individual interleaving
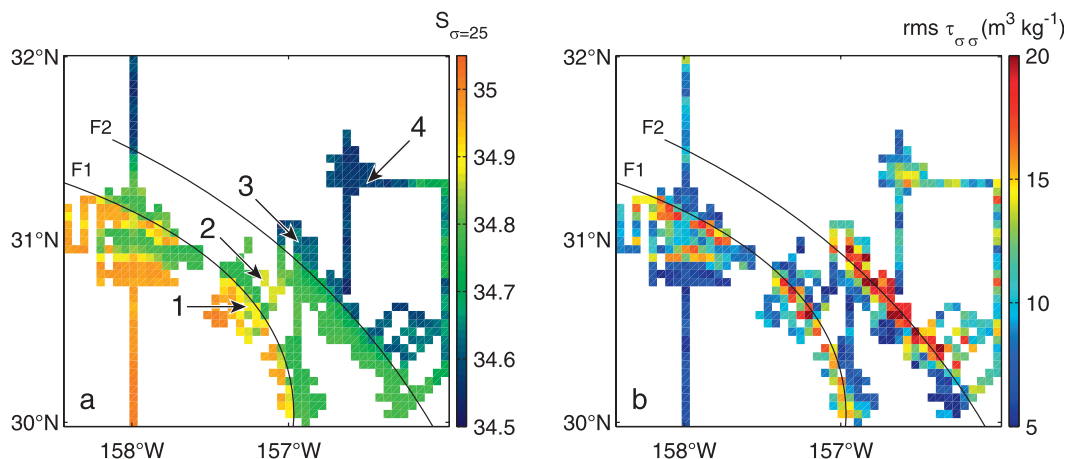
FIG. 9. Distribution of (a) reference salinity at $\sigma_\theta = 25.0$ kg m^{-3} and (b) rms of diapycnal spiciness curvature over the whole vertical extent of SWIMS surveys 5–29 Jul 2007 (in 5 km × 5 km spatial bins). Black lines show approximate location of two main fronts (F1 and F2), visible in isopycnal salinity distribution. Numbered arrows show the location of the features, detailed in Figs. 10 and 11.

features coincide well with the along- or cross-front flow anomalies (Figs. 10c,h). Overall, correlations between the velocity anomalies and intrusions descriptors (salinity anomaly or $\tau_{\sigma\sigma}$) are not statistically significant. The lack of linear correlation highlights the integrating nature of the interleaving, whereby the intrusion amplitude is determined by its advective history. Beal (2007) reports a similar lack of correlation between intrusions and the velocity field in the Agulhas Current.

7. Variability along interleaving layers

a. Layer analysis method

Lateral coherence is an important property distinguishing intrusions from other types of thermohaline fine structure. Once the intrusions have been located at each individual profile, their lateral connectivity needs to be established. This allows additional characterization of the intrusions by their lateral extent, slope, and integral and mean thickness.

Automation of this procedure involves incremental building of continuous strings of minima and maxima. Profiles in each section are considered consecutively, and the local extrema are identified using the multiscale method. If a particular extremum is sufficiently close to the end of an existing string of extrema, both vertically and horizontally, it is added to the string. Only extrema of the same sign belonging to adjacent profiles and separated by less than 0.15 kg m^{-3} in density were connected, a choice that minimizes cross-linking of the layers. If several extrema satisfy these criteria, the closest in density continues the string, and a secondary fork in the string may be marked. Extrema that cannot

be conjoined to existing strings initiate new strings, and short strings that terminate within three points are discarded. The remaining strings are sorted by their weight, defined, for example, as the sum of the heights of the constituting extrema. A similar procedure is described by Richards and Banks (2002); one major distinction of our algorithm is the application of multiscale peak analysis as a first stage, which is an alternative method of "multiple points defining a single maximum or minimum in the vertical [being] reduced to a single point."

An example of layers identified in one of the cross-frontal SWIMS sections is shown in Fig. 13. The abundance of identified coherent layers is a result of applying the new curvature method of intrusion detection. About 80% of these layers would not be identified by the salinity inversion method, and their mean lateral extent would be shortened by a factor of 2. At the same time, laterally coherent salinity inversions followed the high-curvature layers closely wherever they overlapped.

b. Layer properties

Laterally coherent layers of strong diapycnal curvature were identified in 22 sections crossing the F1 front between 13 and 20 July 2007. Only sections of sufficient length (>10 km) and regularity running approximately perpendicular to the front were selected. About 1100 individual layers were found. Of these layers, 51% corresponded to curvature maxima and 49% to minima. Histograms of a few of their key properties are shown in Fig. 14, and their mean, median, and standard deviation values are listed in Table 1.

The average lateral extent of traced layers of curvature extrema was 6.3 km, and 20% of them were longer
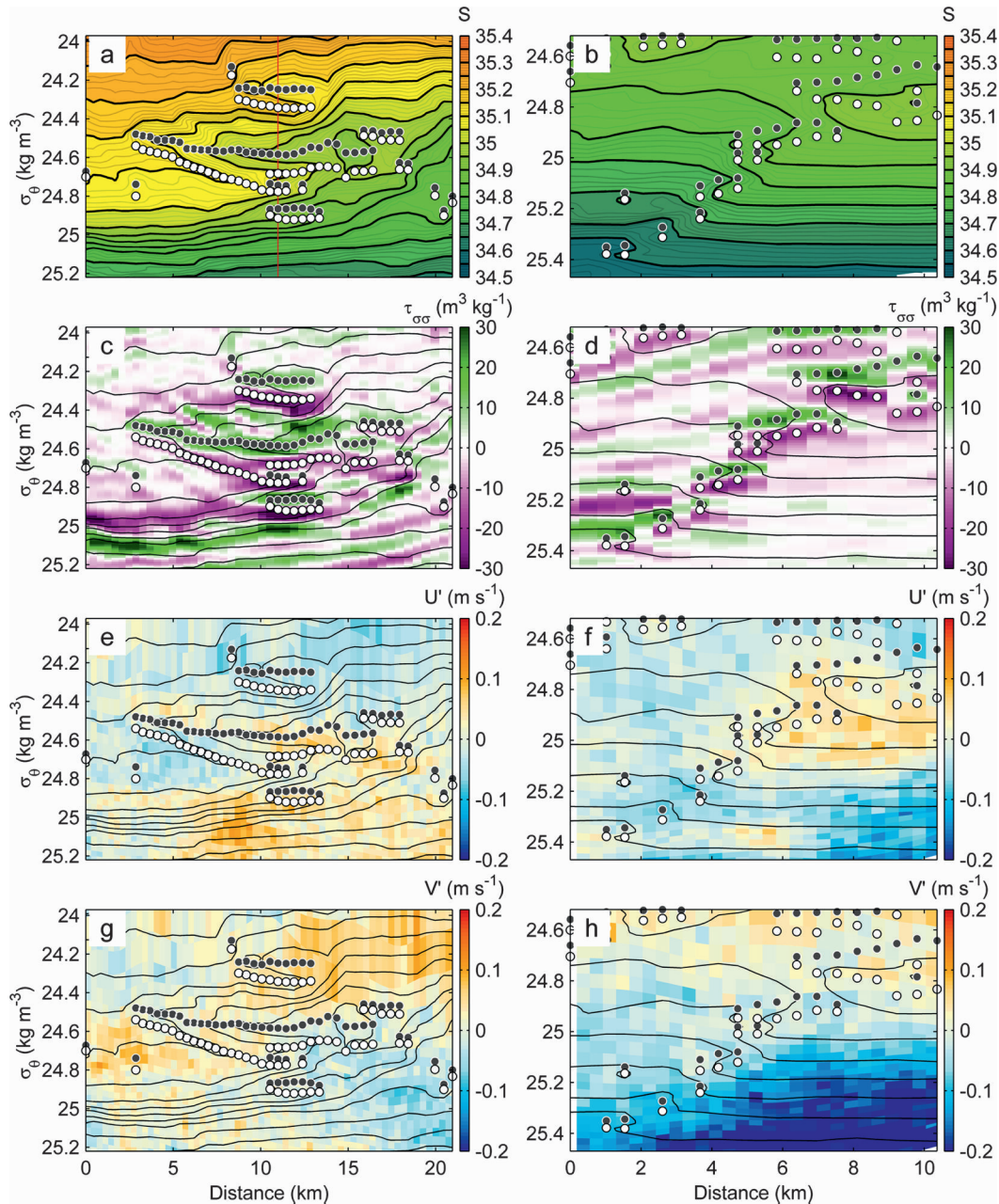
FIG. 10. Two examples of intrusions in the STFZ. Sections of (a),(b) salinity, (c),(d) diapycnal spiciness curvature $\tau_{\sigma\sigma}$, as well as (e),(f) cross-section and (g),(h) along-section velocity anomalies (relative to the upper 100-m average) are shown, overlaid with black isohaline contours. Local salinity minima (maxima) are marked by dark and (light) circles. Columns represent different locations within the 17 Jul 2007 survey: (left) near 30°35′N, 157°17′W, 50−125 dbar (''1'' in Fig. 1), and (right) 30°45′N, 157°10′W, 50−140 dbar (''2'' in Fig. 1). Red line in (a) marks the location of a sample profile, shown in Fig. 12.

than 10 km (Fig. 14a). They were found at all density levels (Fig. 14b), although the deeper ones tended to have slightly greater lateral extent. Because $\tau_{\sigma\sigma}$ variability increased near the fronts and resulted in clustering of $\tau_{\sigma\sigma}$ extrema (see sections 5 and 6), 70% of identified layers lay within 10 km of F1.

Cross-isopycnal slope of the interleaving layers was highly variable (Fig. 14c). On average, the layers were getting denser toward the cold and fresh side of the front, so the mean cross-isopycnal slope of the layers $(\partial\sigma/\partial y)_{\text{layer}}$ was -5.1×10^{-6} kg m^{-4}. The mean of this distribution is significantly different from zero
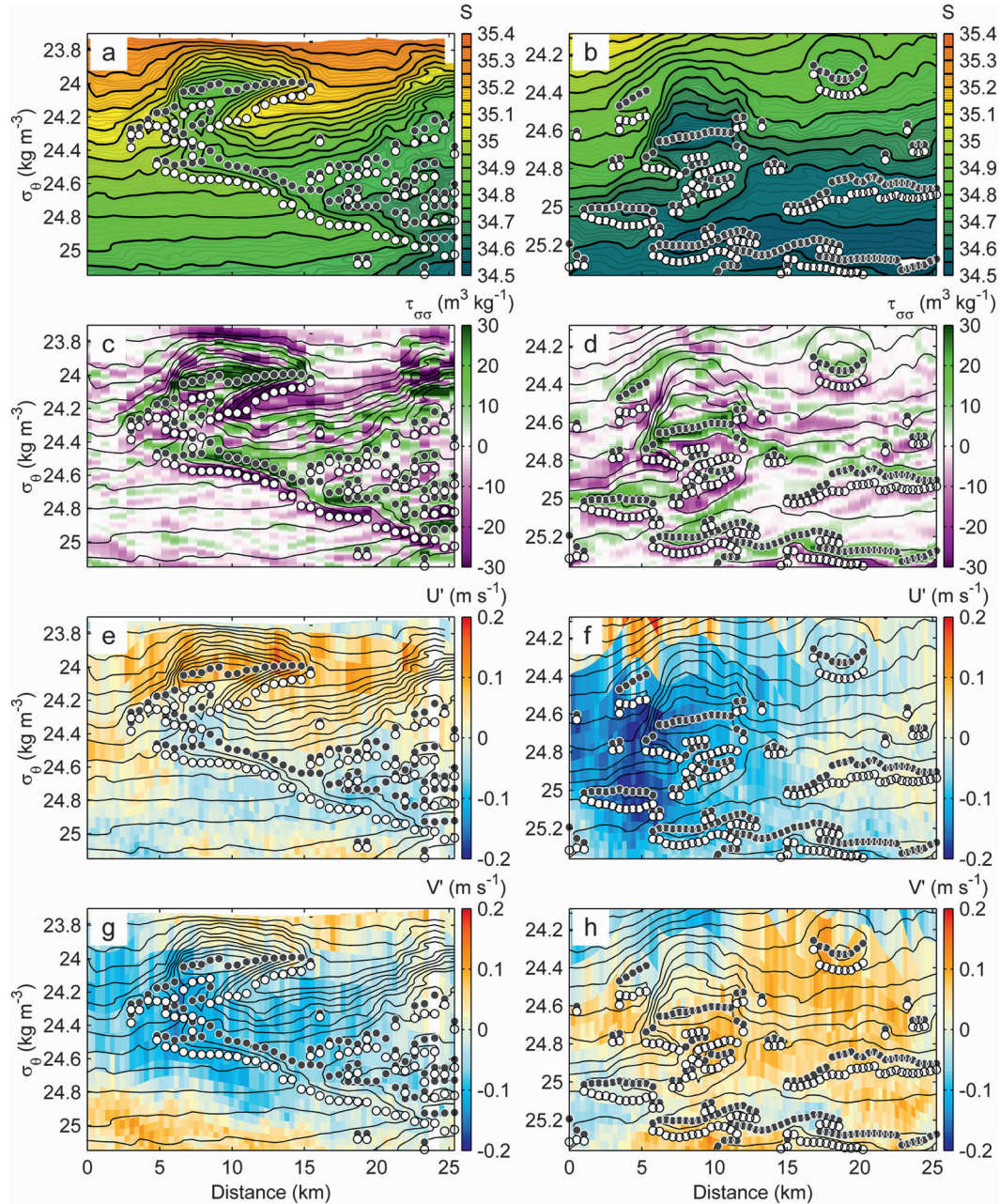
FIG. 11. As in Fig. 10, but for two more examples of intrusions in the STFZ: (left) 30°49′N, 156°57′W at 30−80 dbar on 21 Jul 2007 ("3" in Fig. 1); (right) 31°18′N, 156°24′W at 40−100 dbar on 27 Jul 2007 ("4" in Fig. 1).

(confidence level >99%), despite the relatively high standard deviation of 2.5×10^{-5} kg m^{-4}. Distribution of the slopes of the layers relative to isobars (Fig. 14d) was also quite broad and significantly skewed toward negative values, with the mean slope -1.0×10^{-3} and standard deviation 2.2×10^{-3}. Such a broad spread of the layer slopes argues against the double-diffusive nature of the observed interleaving (see section 9 for further discussion).

Salinity generally decreased along the layers toward the cold and fresh side of the front (Fig. 14c), although the decrease was slower than along the isopycnals. The mean along-layer gradient of salinity $(\partial S/\partial y)_{\text{layer}}$ was -4.2×10^{-6} m^{-1} compared to an average isopycnal value of $(\partial S/\partial y)_\sigma = -1 \times 10^{-5}$ m^{-1} observed between $\sigma_\theta = 24.4$ and 24.8 kg m^{-3}. This observation is consistent with the average slope of the layers being intermediate to those of the isopycnals and the isohalines.
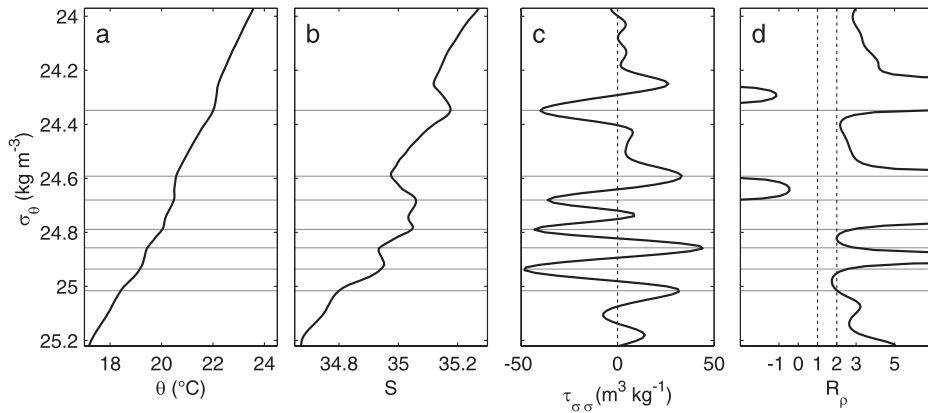
FIG. 12. Profiles of (a) potential density, (b) salinity, (c) diapycnal spiciness curvature, and (d) vertical density ratio. Horizontal lines mark the levels of strong curvature extrema ($|\tau_{\sigma\sigma}| > 30$ m^3 kg^{-1}). Location of the profiles is marked in Fig. 10a.

Another parameter characterizing the layers is the along-intrusion density ratio, defined as

$$R_l = \frac{\alpha}{\beta}\left(\frac{\partial\theta}{\partial S}\right)_{\text{layer}}. \tag{9}$$

This parameter, related to $(\partial\sigma/\partial y)_{\text{layer}}$ and $(\partial S/\partial y)_{\text{layer}}$, is commonly used to check for consistency with the May

and Kelley (2001, hereafter MK01) scaling for a double-diffusively driven interleaving in steady state. The layers observed in the STFZ showed a wide range of along-intrusion density ratios, with a mean of 2.8 and a standard deviation of 2.0 (Fig. 14f). Implications of these observations are discussed in section 9.

Only a small subset (20%) of the coherent layers could be detected by the salinity inversion method. They
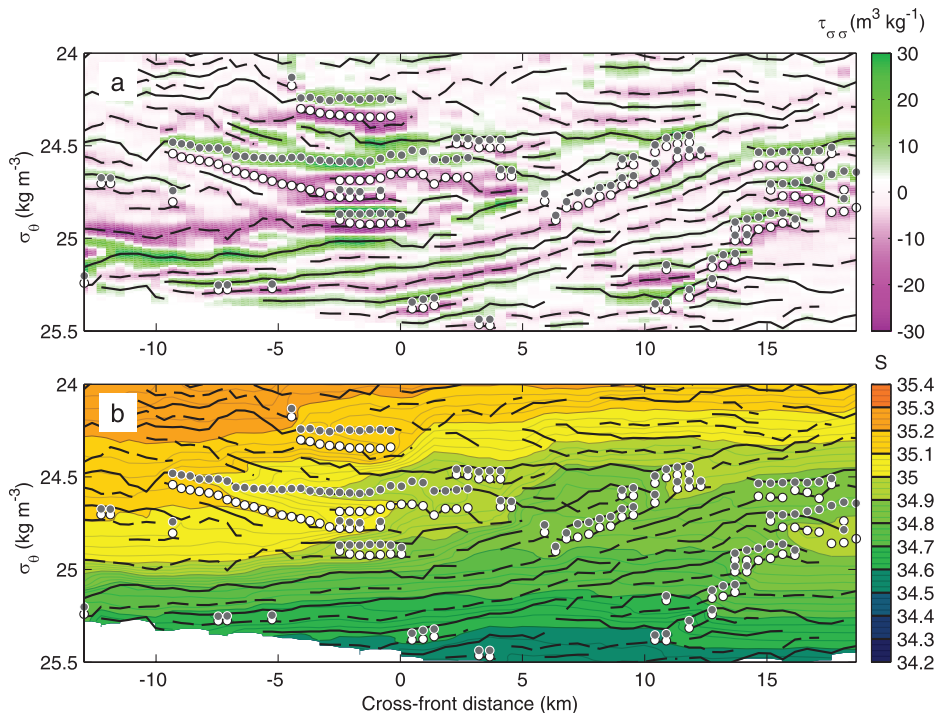

FIG. 13. Interleaving layers marked by the strings of diapycnal spiciness curvature minima (dashed lines) and maxima (solid lines) in one of the cross-frontal SWIMS sections occupied on 17 Jul 2007. The strings are overlaid on the background of (a) spiciness curvature and (b) salinity sections. Local salinity minima and maxima are marked by dark and light circles for comparison.
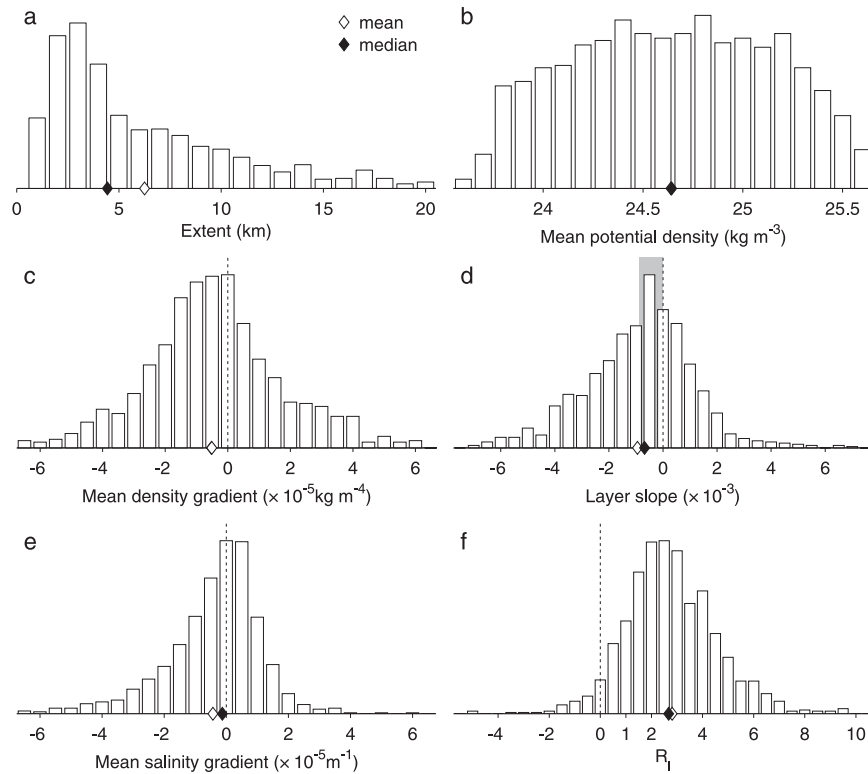
FIG. 14. Histograms of the properties of laterally coherent layers of high absolute curvature: (a) lateral extent, (b) mean potential density, (c) mean along-layer potential density gradient, (d) mean layer slope (pressure gradient), (e) mean along-layer salinity gradient, and (f) along-layer density ratio R_l. The mean and median values are marked by open and solid diamonds on the horizontal axes, and also listed in Table 1. Gray shading in (d) marks the range of slopes of intrusions driven by salt fingering according to MK97.

showed similar statistics (Table 1) with a few notable exceptions. On average, inversion layers were 35% shorter than the layers of high spiciness curvature, as expected from the example shown in Fig. 13. Along-layer gradients of density were somewhat weaker, whereas the gradients of salinity were stronger. The significance of these differences is difficult to judge given the broad and non-Gaussian distributions of the parameters and relatively low number of inversions. Overall, we expect the curvature method to produce a more

faithful description of the statistics of the interleaving layers.

8. Summary

Our recent field observations support reports that the STFZ is the site of numerous thermohaline intrusions with 1–10-km lateral coherence. We showed that salinity inversions are one type in a broader class of distortions in thermohaline structure due to interleaving motions

TABLE 1. Parameters of coherent layers, identified using the spiciness curvature and salinity inversion methods.

	Method					
	Curvature ($n = 1103$)			Inversion ($n = 220$)		
Parameter	Mean	Median	Std dev	Mean	Median	Std dev
L (km)	6.3	4.4	5.0	4.1	3.0	3.2
σ_θ (kg m^{-3})	24.6	24.6	0.5	24.7	24.7	0.4
$(d\sigma/dy)_{\text{layer}}$ ($\times 10^{-5}$ kg m^{-4})	-0.5	-0.5	2.5	-0.3	-0.2	3.0
$(dz/dy)_{\text{layer}}$ ($\times 10^{-3}$)	-1.0	-0.7	2.2	-0.9	-0.8	2.6
$(dS/dy)_{\text{layer}}$ ($\times 10^{-5}$ m^{-1})	-0.4	-0.1	2.0	-0.9	-0.4	2.7
R_l	2.8	2.7	2.0	2.3	2.1	2.2

and not the sole indicator of thermohaline intrusions. A new method to detect these distortions, based on diapycnal spiciness curvature, revealed a greater complexity and horizontal extent of intrusions in the STFZ than obtained with previous methods. The curvature method detected five times as many laterally coherent intrusive layers and was able to track them laterally over a 50% greater distance, compared with the salinity inversion method. Clusters of particularly strong intrusions were preferentially found within 5 km of two thermohaline fronts, where both the lateral salinity gradients and the mesoscale velocity strain were intensified. The vertical scale of the intrusions was on the order of 10 m, even though we showed that this estimate may be partially sensitive to the analysis procedure. The slopes of intrusions with respect to isobars, isopycnals, and isohalines were strongly variable. On average, however, intrusion slopes were intermediate between those of isopycnals and isohalines.

9. Discussion

There are two broad classes of theories on the origins of thermohaline intrusions. ''Active'' theories suggest that intrusions are self-driven, gaining energy from the thermohaline fields via double diffusion of heat and salt (Ruddick and Kerr 2003), or of density and momentum (McIntyre 1970). Various modifications of DD theories have dominated interpretations of intrusion observations for the past 30 years (e.g., Kuzmina and Rodionov 1992; Ruddick 1992; MK97; Smyth 2008). A number of field observations, however, have reported slopes and scales for the intrusive features that are inconsistent with the ''active'' theories (Kuzmina et al. 2005; Beal 2007). Moreover, it is uncertain whether the classical DD instabilities exist in the presence of typical oceanic levels of turbulent mixing (Zhurbas and Oh 2001; Edwards and Richards 2004). ''Passive'' theories ascribe intrusions to differential stirring of preexisting thermohaline gradients by mesoscale eddies (Ferrari and Polzin 2005; Smith and Ferrari 2009) or through inertial instability (Edwards and Richards 2004).

Consistency of observations with the theories of DD origin of the intrusions is customarily established by examining the slope of the features and the along-intrusion density ratio R_l (e.g., MK97; MK01). The former approach tests the compliance with the predictions of a linear stability analysis; the latter verifies the steady-state balance of the along-intrusion advection with diapycnal diffusion, which is expected to be achieved in finite amplitude features. The linear stability analysis implies a clear separation between the characteristic scale of background variability and that of the intru-

TABLE 2. Typical parameters within 10 km of the F1 front between 50 and 120 m. Cross-front coordinate y is directed toward the cold and fresh side of the front.

Parameter	Mean	Std dev
σ_y ($\times 10^{-6}$ kg m^{-4})	9.3	7
σ_z ($\times 10^{-2}$ kg m^{-4})	-1.4	0.5
S_y ($\times 10^{-5}$ m^{-1})	-1.5	1
S_z ($\times 10^{-3}$ m^{-1})	5.5	2
s_σ ($\times 10^{-4}$)	-7.1	4
s_S ($\times 10^{-3}$)	-2.8	2
R_ρ	4.7	2

sions. Unlike the Meddy Sharon and deep Arctic intrusions, analyzed by MK97 and MK01, such a separation is absent in observations of frontal intrusions. As a result, the definition of the relevant mean background gradient for our observations is not clear, and the overall applicability of this method to frontal regions appears questionable.

We nonetheless performed the analysis of the intrusion slopes using the range of thermohaline gradient values observed between 50 and 100 m within 5 km of F1 (Table 2). According to linear stability theory (MK97) appropriate to baroclinic fronts, initial growth of DD interleaving driven by salt fingering is possible only if the cross-frontal slope of the intrusions relative to isobars, s_i, is between 0 and the critical slope:

$$s_i^* = \frac{\varepsilon_z s_S + s_\sigma}{\varepsilon_z + 1}, \tag{10}$$

where $s_S \equiv \overline{S}_y / \overline{S}_z$ and $s_\sigma \equiv \overline{\sigma}_y / \overline{\sigma}_z$ are the cross-front slopes of background isohalines and isopycnals, respectively; $\varepsilon_z = (1 - \gamma_f)/(R_\rho - 1)$, $\gamma_f = 0.6 \pm 0.2$ is the temperature–salinity flux ratio for salt fingering. For the observed gradients (Table 2), the critical slope of DD interleaving is $s_i^* = (-8.8 \pm 5) \times 10^{-4}$. The slope of the most unstable intrusion for these conditions is $(-4.7 \pm 2) \times 10^{-4}$ and its e-folding growth rate is on the order of 1/60 day^{-1} (see MK97 for details). It can be seen that the range of the observed intrusion slopes (Fig. 14d) is much broader than allowed by linear theory. Moreover, 33% of observed layers had a slope of the opposite sign, $s > 0$ (Fig. 14d). Conceivably, broadening of the range of the intrusion slopes could be attributed to their variable orientation with respect to the front. Double-diffusive interleaving with nonzero alongfront slope, however, would not have a chance to grow appreciably since the characteristic rate of their rotation by the sheared background flow $\overline{v}_z = O(1 \text{ day}^{-1})$ is much faster than their growth rate (MK97). The expected vertical scale of the DD intrusions is roughly set by the Ekman scale $2\pi(A/f)^{1/2} = O(1 \text{ m})$, where $A = O(10^{-5} \text{ m}^2 \text{ s}^{-1})$
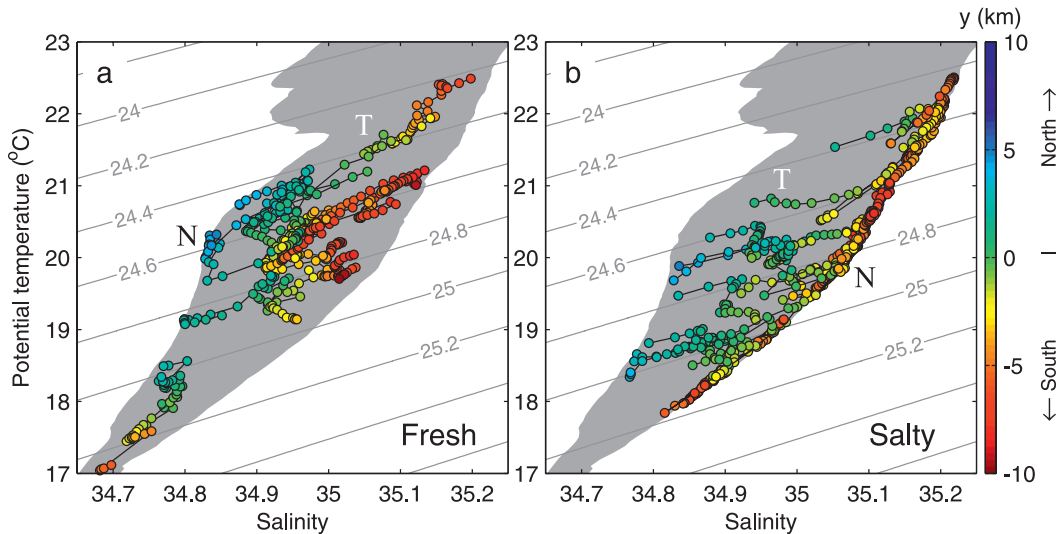
FIG. 15. Evolution of temperature and salinity along the layers of (a) maxima and (b) minima in diapycnal spiciness curvature (low and high salinity intrusions, respectively). Color of the data points correspond to their cross-front location; black lines connect the points belonging to the same intrusion trace. Gray shading shows the envelope of θ–S diagrams. Isopycnal contours are also shown. Native (N) and transitional (T) branches of θ–S traces discussed in the text. The data were obtained during eight crossings of the F1 front on 14 Jul 2007 at approximately 31°09′N, 158°03′W.

is the vertical eddy viscosity and $f = 7.4 \times 10^{-5}$ s^{-1} is the local Coriolis frequency. This estimate is somewhat lower than the thickness of the intrusions targeted by this study, $O(10$ m$)$.

Investigation of the mean along-layer gradients does not give a full account of the variation of thermohaline properties within the layers, as it is often nonuniform. The character of these variations is clearly revealed by θ–S diagrams of the layer properties (Fig. 15). The layers of maximum curvature often had two distinct branches: "native" and "transitional." Native branches (marked "N" in Fig. 15) followed the steep θ–S profiles of either of the water masses separated by the front; transitional branches "T" crossed the area between the two masses. A similar decomposition into "root" (N) and "exchange" (T) branches was introduced by Panteleev and Okhotnikov (2003, hereafter PO03) to classify variations in thermohaline properties along intrusions observed in the Gulf Stream frontal zone. They concluded that changes in the along-intrusion density ratio (and the slope of θ–S diagram) must correspond to the shifts between turbulent and double-diffusive exchange processes. The PO03 analysis followed the finite-amplitude theory of MK01 built upon the assumption of steady-state balance of along-intrusion advection and cross-intrusion mixing. However, the existence of such balance is difficult to verify, and no argument is made in PO03 to support it. In contrast, if the shape and the location of the intrusion core is set by some exogenous advection (see example

below) and not by DD instability, conclusions derived from the along-intrusion density ratios would be misleading. It can be shown that multibranch θ–S tracks, similar to those observed in this study and by PO03, can be obtained by sampling the frontal zone along different paths in the cross-frontal plane (Fig. 16). The characteristic shape of the θ–S tracks is, indeed, determined by the way the features cross the frontal zone, but the dynamics of these features cannot be derived from the along-intrusion density ratio alone. However, this does not imply that the double-diffusive effects can be completely discounted. Divergence of diffusive fluxes of heat and salt through the upper and lower boundaries of the intrusions will affect their dynamics. Unfortunately, the relative importance of DD cannot be assessed before other dynamical contributions are parameterized.

The alternative hypothesis of passive intrusion formation by differential stirring is plausible. Our observations showed that thermohaline fields in the STFZ were strongly deformed at lateral scales on the order of 1–100 km (Figs. 1, 2, 8), suggesting active turbulent stirring. A double cascade of density and spice variance (Klein et al. 1998; Smith and Ferrari 2009) is expected to produce thermohaline filaments of increasingly small vertical and horizontal scales. The intrusions observed may have been a particular case of such three-dimensional filamentation. "Folding" of thermohaline fields by ageostrophic circulation within the unstable fronts as a mechanism for formation of intrusions was proposed by Woods
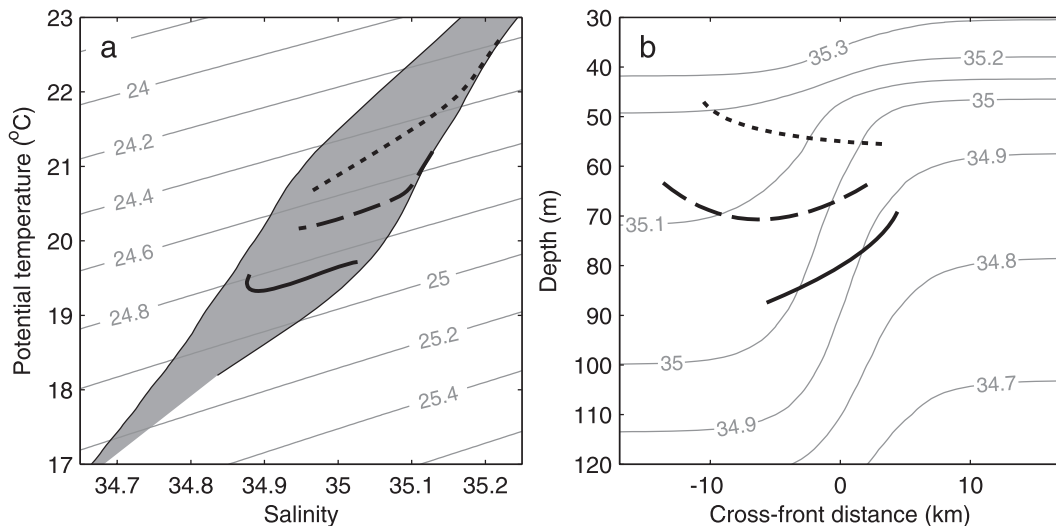
FIG. 16. Dependence of the shape of (a) $\theta-S$ diagram curves (thick lines) on (b) the path of sampling through the frontal zone (thick lines). Various shapes of $\theta-S$ curves resembling those found along the interleaving layers (Fig. 15) may be obtained simply by sampling the fields of an unperturbed idealized front similar to F1 along freely selected smooth paths. Contours of constant potential density and salinity are shown in the background of (a) and (b), respectively. Gray shading in (a) shows the envelope of $\theta-S$ diagrams.

et al. (1977). MacVean and Woods (1980) also showed that folding may occur in stable frontogenesis as well. The hypothesis of turbulent origin of the observed intrusions cannot be readily validated, and deserves further investigation in another study.

The laterally coherent interleaving features found in fields of diapycnal spiciness curvature bear strong resemblance to the banded structures observed in sections of seismic reflection imaging near the water mass boundaries (Nandi et al. 2004). Both approaches show the richness of small-scale filamentation of tracers in frontal zones. Note that seismic imaging responds to the local discontinuities of the sound speed profile, resulting from both the internal waves and density-compensated interleaving features (Nandi et al. 2004). On the other hand, the diapycnal spiciness curvature analysis presented here is less influenced by internal wave heaving and emphasizes the effects of isopycnal processes. We draw attention to the similarity of the features highlighted by these methods to foster complementary interpretation.

The role of observed thermohaline intrusions in the water mass exchange remains unclear. Lateral mixing on scales of 10 m to 10 km is thought to be achieved by the vertical mixing of tracer fields strained by mesoscale eddies, internal waves, and vortical modes (Polzin and Ferrari 2004; Garrett 2006). The observed thermohaline intrusions could contribute to lateral mixing by enhancing vertical thermohaline gradients. To first order, the amount of this contribution is proportional to the lifespan of an intrusion, normalized by the diffusive time scale $t_K = H^2/K$, where H is the intrusion thickness and K is vertical diffusivity. Assuming typical open ocean diffusivity $K = O(10^{-5} \text{ m}^2 \text{ s}^{-1})$ and characteristic intrusion thickness of $H = O(10 \text{ m})$, t_K is of the order of 100 days. Consequently, if the intrusions are rapidly evolving distortions of the thermohaline field caused by internal wave shear, they are likely to be unaffected by mixing; that is, they are "reversible." Only intrusions created by relatively slow submesoscale processes are expected to contribute to lateral mixing. Some of the strongest intrusions observed during the present experiment (e.g., Fig. 10a) were tracked over the period of two weeks, suggesting it may be somewhat "irreversible," thus contributing to lateral mixing. A detailed investigation of the temporal evolution of the intrusion in the STFZ and analysis of the vertical mixing observations made during the experiment in the vicinity of the intrusions are subjects of other studies.
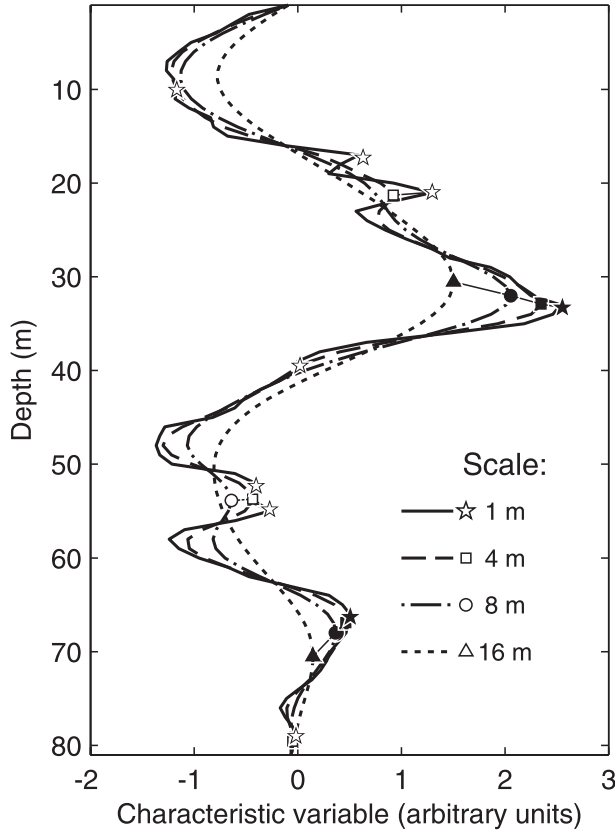
FIG. A1. Multiscale peak analysis procedure applied to a sample profile. Original profile (solid line) and the profiles smoothed with progressively wider filter (other line styles) have different local maxima (symbols). Maxima at $z = 33$ and $z = 66$ (solid stars) "survive" the smoothing with a low-pass filter with half width of 16 m and are thus considered to be the "true" maxima.

APPENDIX A

Multiscale Peak Analysis

Intrusions are detected and characterized in a peak analysis by describing local extrema (minima and maxima) in noisy vertical profiles of a variable such as salinity, temperature, or spiciness anomaly.

Preliminary profile smoothing eliminates spurious extrema, but also shifts peak locations and amplitudes. To address this, multiscale peak analysis identifies original profile extrema and selects the most prominent peaks by successive smoothing (Fig. A1). At each iteration, the original profile is low passed with an increasing filter width. The filter shape is not critical; we use a Blackman filter with weights given by

$$w(z) = 0.42 + 0.5\cos\left(\frac{\pi z}{l}\right)$$
$$+ 0.08\cos\left(\frac{2\pi z}{l}\right), \quad z \in [-l, l], \quad \text{(A1)}$$
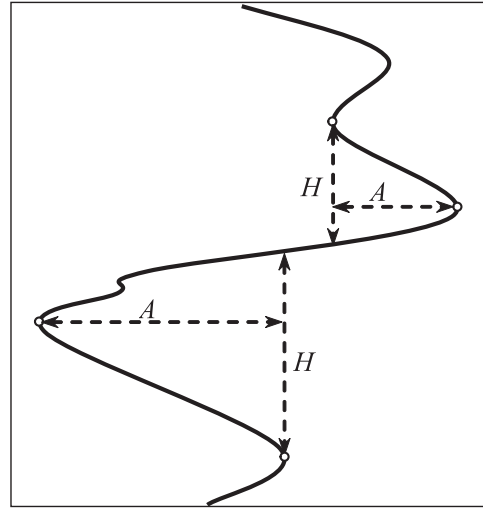

FIG. A2. Determining the thickness (H) and amplitude (A) of a peak or valley. Dots show local minima and maxima obtained by multiscale peak analysis.

and half-width $l = 0, 2, 4, 8, \ldots, L$ grid points ($l = 0$ is no smoothing). Local scale-l maxima are then determined by fitting a second degree interpolating polynomial to each triplet of points in the smoothed profiles. The number of maxima detected at each iteration decreases as the profile becomes progressively smoother. The most prominent maxima persist to larger smoothing scales. Iteration continues to a preset maximum smoothing scale, L. The remaining maxima are traced back to their "ancestors"—the corresponding maxima of the unsmoothed (scale 0) profile, selecting the largest maximum where ancestory is ambiguous (e.g., scale-8 maximum at $z = 54$ m in Fig. A1 has two scale-0 ancestors). The location and maximum values of the selected scale-0 ancestors are then the final result of the algorithm.

Each peak can also be characterized by its amplitude and thickness—nonlocal parameters, determined with respect to its surroundings (Fig. A2). The amplitude of a peak is defined as the difference between the peak maximum and the nearest local minimum. The thickness of the peak is the vertical distance between the nearest minimum and its projection to the profile on the opposite side of the peak. Because these two peak parameters are defined with respect to the neighboring valley, they can change drastically depending on the criteria of extrema detection. Multiscale peak analysis reduces this sensitivity by eliminating the spurious extrema attributable to small-scale noise. Peak rejection criteria are still dependent on the choice of a maximum smoothing scale L; this dependence is investigated in section 3c.
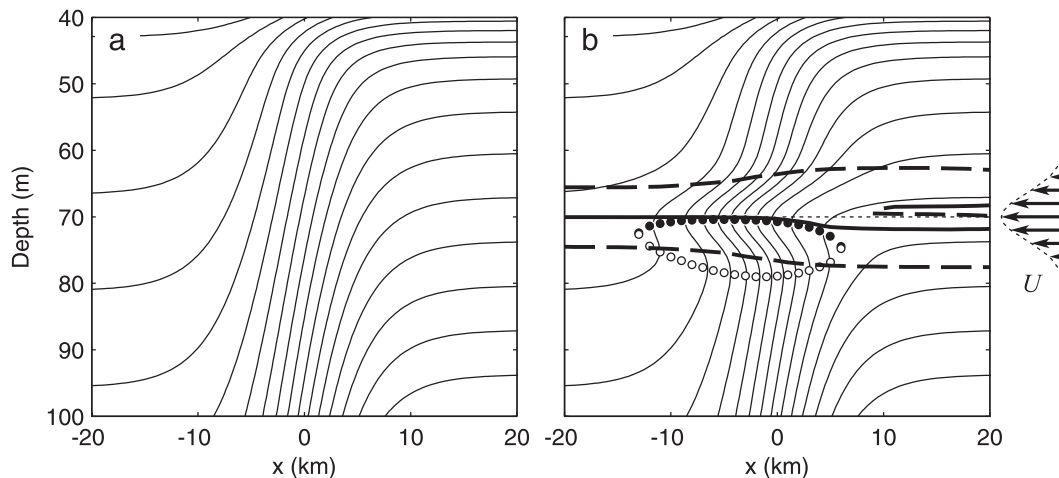
FIG. B1. Synthetic example of intrusion formation. (a) Initial and (b) distorted salinity fields are shown. Vertical profile of advection velocity is shown in the right margin. Two methods of intrusion detection are applied to the salinity field in (b): salinity minima and maxima are marked by solid and open circles; diapycnal spiciness curvature $\tau_{\sigma\sigma}$ minima and maxima are marked by heavy dashed and solid lines, respectively. Notice that the $\tau_{\sigma\sigma}$ maximum follows the advected intrusion core more faithfully than the salinity minimum.

APPENDIX B

Validation of Curvature Method with Synthetic Data

The performance of the intrusion detection methods can be compared using a synthetic example of a lateral intrusion. Initial sections of temperature and salinity represent an idealized version of the observed STFZ, centered at $x = 0$ (Fig. B1a). For simplicity, this front is fully compensated laterally so that the density is a function of depth only. Deformation of the thermohaline field in response to localized cross-frontal intrusive advection at $z_0 = 70$ m was modeled analytically in two dimensions. Figure B1b shows the deformed salinity field after 12 h of advection with a Gaussian velocity profile $u(z) = u_0 \exp\{-[(z - z_0)/L_u]^2\}$, where $u_0 = -0.1$ m s^{-1} and $L_u = 5$ m. By design, vertical density stratification does not change while a low-salinity intrusion forms in the frontal zone. The intrusion detection algorithms should be able to recover the depth of the advective core of the intrusion (70 m) in each vertical profile.

The inversion method detects the core and the bottom of the intrusion but only in the central zone of the front (Fig. B1b). Salinity inversion only develops in the strongest horizontal gradients (-10 km $< x < 4$ km), even though the advection clearly disturbs the profiles across the entire front (Fig. B1b). The location of the intrusion core inferred from the salinity minimum and the intrusion thickness from the vertical distance between salinity extrema vary with the local changes in the

shape of the salinity profile. These variations are potentially misleading with respect to the intrusion formation process because the advection field does not vary laterally.

The curvature method of the characterization of this model intrusion is not limited to the area of the inversion, and can track the intrusion core throughout most of the domain. Curvature-based intrusion detection is more sensitive than visual detection, especially where the latter is complicated by strong vertical gradients. In the idealized case considered here, even small lateral gradients produce a perceptible change of curvature. Although in practice these changes may be easily obscured by the instrumental noise or scalar turbulence, the sensitivity of the curvature method is still expected to surpass that of the peak analysis methods.

The curvature method also locates the core of the advected patch at the maximum in $\tau_{\sigma\sigma}$ (Fig. B1b, solid line), whose depth remains fairly constant across the domain (70.3 ± 1.2 m) and lies close to the maximum advection at 70 m. Both upper and lower boundaries of the advected patch are demarcated by the local peaks of negative curvature (Fig. B1b, dashed line), in contrast to the inversion method that only detects one. Even though the vertical separation between the two boundaries varies, it shows much less artificial change than is evident in the inversion method.

Curvature profiles through the rightmost side of the synthetic intrusion exhibit broad peaks at the intrusion depth, leading to splitting of the maxima that correspond to the intrusion core (Fig. B1b). This structure is an example of a relatively thick intrusion (similar to that

shown in Fig. 6b), created where the displacement due to lateral advection exceeds the scale of local salinity variation. Such an intrusion exhibits a relatively featureless core of foreign stratification embedded in the surrounding waters. Curvature maxima mark the vertical extent of this core.

These observations reemphasize the remark of caution regarding potential mismatch between the locations of advection and curvature maxima. Vertical alignment of the two maxima is only expected under a steady balance of advection and diffusion, a condition clearly not satisfied by the analytical model, which lacks mixing. Including weak vertical salinity diffusivity $K = 3 \times 10^{-5}$ m^2 s^{-1} in the synthetic intrusion model produces a curvature distribution with a single maximum at 70.5 ± 0.6 m. Increasing diffusivity to 3×10^{-4} m^2 s^{-1} further improves correspondence between the location of the curvature maximum (70.1 ± 0.1 m) and the level of maximum advection (70 m), reducing both the bias and the standard deviation of the discrepancy.

APPENDIX C

Minimal Intrusion to Produce Salinity Inversion

How large must an intrusion be to produce an inversion of a salinity profile? Consider a linear background salinity profile $\overline{S}(\sigma)$ such that $\overline{S}_\sigma = $ const, superimposed with periodic salinity anomaly $\Delta S = S_i \sin(2\pi\sigma/H)$, where S_i is the salinity anomaly amplitude and H is the characteristic diapycnal thickness of the intrusions. Salinity inversions would form if

$$\frac{d}{d\sigma}(\overline{S} + \Delta S) = \overline{S}_\sigma + \frac{2\pi S_i}{H}\cos\frac{2\pi\sigma}{H} \qquad (C1)$$

changes sign, which is only possible if the intrusion amplitude exceeds a critical value S_i^*:

$$S_i > S_i^* = \left|\frac{H\overline{S}_\sigma}{2\pi}\right|. \qquad (C2)$$

A sinusoidal intrusion profile with this critical intrusion amplitude has the diapycnal salinity curvature amplitude $S_{\sigma\sigma}^* = 4\pi^2 S_i^*/H^2$, which can be related to the critical spiciness curvature, $\tau_{\sigma\sigma}^*$, using (8):

$$\tau_{\sigma\sigma}^* \approx 2\beta\rho S_{\sigma\sigma}^* = 4\pi\beta\rho\frac{\overline{S}_\sigma}{H}. \qquad (C3)$$

For the typical values of $S_\sigma = -0.3$ m^3 kg^{-1} ($R_\rho = 5$), observed in the upper thermocline just south of the STFZ, and intrusion thickness $H = 0.1$ kg m^{-3} (about 8 m), we obtain $S_i^* = 5 \times 10^{-3}$ and $\tau_{\sigma\sigma}^* = 28$ m^3 kg^{-1}.

The relationship between the emergence of salinity inversions and the value of the nearby spiciness curvature extremum depends on the shape of the $\Delta S(\sigma)$ profile, so critical values obtained for sinusoidal ΔS give only a rough guide. For example, from Fig. 5 it is evident that salinity inversions may occasionally be associated with curvature extrema of less than 20 m^3 kg^{-1}.

REFERENCES

Beal, L. M., 2007: Is interleaving in the Agulhas Current driven by near-inertial velocity perturbations? *J. Phys. Oceanogr.,* **37,** 932–945.

Edwards, N. R., and K. J. Richards, 2004: Nonlinear double-diffusive intrusions at the equator. *J. Mar. Res.,* **62,** 233–259.

Fedorov, K. N., 1978: *The Thermohaline Finestructure of the Ocean.* Pergamon Press, 170 pp.

Ferrari, R., and D. L. Rudnick, 2000: Thermohaline variability in the upper ocean. *J. Geophys. Res.,* **105,** 16 857–16 883.

——, and K. L. Polzin, 2005: Finescale structure of the *T–S* relation in the eastern North Atlantic. *J. Phys. Oceanogr.,* **35,** 1437–1454.

Flament, P., 2002: A state variable for characterizing water masses and their diffusive stability: Spiciness. *Prog. Oceanogr.,* **54,** 493–501.

Garrett, C., 2006: Turbulent dispersion in the ocean. *Prog. Oceanogr.,* **70,** 113–125.

Gregg, M. C., 1975: Microstructure and intrusions in the California Current. *J. Phys. Oceanogr.,* **5,** 253–278.

Joyce, T. M., 1977: A note on the lateral mixing of water masses. *J. Phys. Oceanogr.,* **7,** 626–629.

Klein, P., A. M. Treguier, and B. L. Hua, 1998: Three-dimensional stirring of thermohaline fronts. *J. Mar. Res.,* **56,** 589–612.

Kuzmina, N., and V. B. Rodionov, 1992: Influence of baroclinicity on formation of thermohaline intrusions in ocean frontal zones. *Izv., Atmos. Oceanic Phys.,* **28,** 804–810.

——, B. Rudels, T. Stipa, and V. Zhurbas, 2005: The structure and driving mechanisms of the Baltic intrusions. *J. Phys. Oceanogr.,* **35,** 1120–1137.

MacVean, K., and J. D. Woods, 1980: Redistribution of scalar during upper ocean frontogenesis: A numerical model. *Quart. J. Roy. Meteor. Soc.,* **106,** 293–312.

May, B. D., and D. E. Kelley, 1997: Effect of baroclinicity on double-diffusive interleaving. *J. Phys. Oceanogr.,* **27,** 1997–2008.

——, and ——, 2001: Growth and steady state stages of thermohaline intrusions in the Arctic Ocean. *J. Geophys. Res.,* **106,** 16 783–16 794.

McDougall, T. J., 1984: The relative roles of diapycnal and isopycnal mixing on subsurface water mass conversion. *J. Phys. Oceanogr.,* **14,** 1577–1589.

——, and A. B. Giles, 1987: Migration of intrusions across isopycnals, with examples from the Tasman Sea. *Deep-Sea Res.,* **34,** 1851–1866.

McIntyre, M. E., 1970: Diffusive destabilization of the baroclinic circular vortex. *Geophys. Fluid Dyn.,* **1,** 19–57.

Morison, J., R. Andersen, N. Larson, E. Asaro, and T. Boyd, 1994: The correction for thermal-lag effects in Sea-Bird CTD data. *J. Atmos. Oceanic Technol.,* **11,** 1151–1164.

Mueller, R. D., W. D. Smyth, and B. Ruddick, 2007: Shear and convective turbulence in a model of thermohaline intrusions. *J. Phys. Oceanogr.,* **37,** 2534–2549.

Nandi, P., W. S. Holbrook, S. Pearse, P. Páramo, and R. W. Schmitt, 2004: Seismic reflection imaging of water mass boundaries

in the Norwegian Sea. *Geophys. Res. Lett.,* **31,** L23311, doi:10.1029/2004GL021325.

Panteleev, N. A., and I. N. Okhotnikov, 2003: Intrusive Stratification of the Gulf-Stream Frontal Zone According to the Results of Investigations Performed during Cruise 43 of the R/V *Akademik Vernadskii. Phys. Oceanogr.,* **13,** 104–115.

Polzin, K., and R. Ferrari, 2004: Isopycnal dispersion in NATRE. *J. Phys. Oceanogr.,* **34,** 247–257.

Richards, K., and H. Banks, 2002: Characteristics of interleaving in the western equatorial Pacific. *J. Geophys. Res.,* **107,** 3231, doi:10.1029/2001JC000971.

Roden, G. I., 1964: Shallow temperature inversions in the Pacific Ocean. *J. Geophys. Res.,* **69,** 2899–2914.

——, 1980: Variability of surface temperature fronts in the western Pacific, as detected by satellite. *J. Geophys. Res.,* **85,** 2704–2710.

——, 1981: Mesoscale thermohaline, sound velocity and baroclinic flow structure of the Pacific subtropical front during the winter of 1980. *J. Phys. Oceanogr.,* **2,** 658–675.

Ruddick, B., 1983: A practical indicator of the stability of the water column to double-diffusive activity. *Deep-Sea Res.,* **30,** 1105–1107.

——, 1992: Intrusive mixing in a Mediterranean salt lens—Intrusion slopes and dynamical mechanisms. *J. Phys. Oceanogr.,* **22,** 1274–1285.

——, and O. Kerr, 2003: Oceanic thermohaline intrusions: Theory. *Prog. Oceanogr.,* **56,** 483–497.

——, O. M. Phillips, and J. S. Turner, 1999: A laboratory and quantitative model of finite-amplitude thermohaline intrusions. *Dyn. Atmos. Oceans,* **30,** 71–99.

Schmitt, R. W., 1981: Form of the temperature-salinity relationship in the central water: Evidence for double-diffusive mixing. *J. Phys. Oceanogr.,* **11,** 1015–1026.

——, 2003: Observational and laboratory insights into salt finger convection. *Prog. Oceanogr.,* **56,** 419–433.

Smith, K. S., and R. Ferrari, 2009: The production and dissipation of compensated thermohaline variance by mesoscale stirring. *J. Phys. Oceanogr.,* in press.

Smyth, W. D., 2008: Instabilities of a baroclinic, double diffusive frontal zone. *J. Phys. Oceanogr.,* **38,** 840–861.

Stommel, H., and K. N. Fedorov, 1967: Small-scale structure in temperature and salinity near Timor and Mindanoa. *Tellus,* **19,** 76–81.

Takeuchi, K., 1984: Numerical study of the Subtropical Front and the Subtropical Countercurrent. *J. Oceanogr.,* **40,** 371–381.

Toole, J. M., 1981: Intrusion characteristics in the Antarctic Polar Front. *J. Phys. Oceanogr.,* **11,** 780–793.

Woods, J. D., R. L. Wiley, and M. G. Briscoe, 1977: Vertical circulation at fronts in the upper ocean. *Deep-Sea Res.,* **24** (Suppl.), 253–275.

Yuan, X., and L. D. Talley, 1992: Shallow salinity minima in the North Pacific. *J. Phys. Oceanogr.,* **22,** 1302–1316.

Zhurbas, V., and I. S. Oh, 2001: Can turbulence suppress double-diffusively driven interleaving completely? *J. Phys. Oceanogr.,* **31,** 2251–2254.

Zika, J. D., and T. J. McDougall, 2008: Vertical and lateral mixing processes deduced from the Mediterranean Water signature in the North Atlantic. *J. Phys. Oceanogr.,* **38,** 164–176.